AGU PUBLICATIONS

Geochemistry, Geophysics, Geosystems

RESEARCH ARTICLE
10.1002/2015GC005943

Special Section:
The Lithosphere-asthenosphere System

Characterization and Petrological Constraints of the Midlithospheric Discontinuity

Erika Rader[1], Erica Emry[2], Nicholas Schmerr[3], Daniel Frost[4], Cheng Cheng[5], Julie Menard[1], Chun-Quan Yu[6], and Dennis Geist[7]

[1]Department of Biodiversity, Earth, and Environmental Sciences, Academy of Natural Sciences of Drexel University, Philadelphia, Pennsylvania, USA, [2]Department of Geosciences, Penn State University, University Park, Pennsylvania, USA, [3]Department of Geology, University of Maryland, College Park, Maryland, USA, [4]School of Earth and Environment, University of Leeds, Leeds, UK, [5]Department of Earth and Planetary Science, University of California Berkeley, Berkeley, California, USA, [6]Department of Earth, Atmospheric and Planetary Sciences, Massachusetts Institute of Technology, Cambridge, Massachusetts, USA, [7]Department of Geological Sciences, University of Idaho, Moscow, Idaho, USA

Key Points:
- MLD is found at consistent depths below cratons
- Xenoliths from this horizon contain hydrous minerals
- Hydrous minerals are trapped when melt cools

Supporting Information:
- Supporting Information S1

Correspondence to:
E. Rader,
elr56@drexel.edu

Citation:
Rader, E., E. Emry, N. Schmerr, D. Frost, C. Cheng, J. Menard, C.-Q. Yu, and D. Geist (2015), Characterization and Petrological Constraints of the Midlithospheric Discontinuity, *Geochem. Geophys. Geosyst.*, *16*, doi:10.1002/2015GC005943.

Received 10 JUN 2015
Accepted 26 AUG 2015
Accepted article online 1 SEP 2015

Abstract Within continental lithosphere, widespread seismic evidence suggests a sharp discontinuous downward decrease in seismic velocity at 60–160 km depth. This midlithospheric discontinuity (MLD) may be due to anisotropy, melt, hydration, and/or mantle metasomatism. We survey global seismologic observations of the MLD, including observed depths, velocity contrasts, gradients, and locales across multiple seismic techniques. The MLD is primarily found in regions of thick continental lithosphere and is a decrease in seismic shear velocity (2–7% over 10–20 km) at 60–160 km depth, the majority of observations clustering at 80–100 km. Of xenoliths in online databases, 25% of amphibole-bearing xenoliths, 90% of phlogopite-bearing xenoliths, and none of carbonate-bearing xenoliths were formed at pressures associated with these depth (2–5 GPa). We used Perple_X modeling to evaluate the elastic moduli and densities of multiple petrologies to test if the MLD is a layer of crystallized melt. The fractional addition of 5–10% phlogopite, 10–15% carbonate, or 45–100% pyroxenite produce a 2–7% velocity decrease. We postulate this layer of crystallized melt would originate at active margins of continents and crystallize in place as the lithosphere cools. The concentration of mildly incompatible elements (Y, Ho, Er, Yb, and Lu) in xenoliths near the MLD is consistent with higher degrees of melting. Thus, we postulate that the MLD is the seismological signature of a chemical interface related to the paleointersection of a volatile-rich solidus and progressively cooling lithosphere. Furthermore, the MLD may represent a remnant chemical tracer of the lithosphere-asthenosphere boundary (LAB) from when the lithosphere was active and young.

1. Introduction

Seismological investigations of continental lithosphere have uncovered substantial evidence for the presence of a discontinuous seismic velocity reduction between 60 and 160 km depth [e.g., *Fischer et al.*, 2010]. This discontinuity falls within the elevated velocities of the tomographically defined lithosphere but resembles the downward velocity reduction often associated with the lithosphere-asthenosphere boundary (LAB) [e.g., *Rychert et al.*, 2005]. The intralithosphere velocity reduction has been deemed "the mid-lithospheric discontinuity" (MLD) [*Wirth and Long*, 2014; *Fischer et al.*, 2010; *Yuan and Romanowicz*, 2010] (Figure 1). Detections of the MLD span a wide suite of seismic methods, including long-range, active-source seismic refractions [*Thybo and Perchuc*, 1997], shear wave anisotropy [*Yuan et al.*, 2011], P and S receiver functions [e.g., *Rychert et al.*, 2005; *Savage and Silver*, 2008; *Abt et al.*, 2010; *Ford et al.*, 2010], SS and PP precursors [*Heit et al.*, 2010, Shearer, 1993, *Zheng and Romanowicz*, 2012], ScS core-reflected phases [*Courtier and Revenaugh*, 2006], and surface wave tomography [e.g., *Adams et al.*, 2012; *Fishwick and Rawlinson*, 2012; *Heeszel et al.*, 2013; *Jiang et al.*, 2013].

A variety of mechanisms have been proposed to explain the origin of the observed velocity reduction at the MLD (and/or the LAB), including (1) the presence of modern carbonatite [*Dasgupta and Hirschmann*, 2010], silicate [*Dasgupta et al.*, 2013], or sulfidic [*Helffrich et al.*, 2011] melts near the depth of the interface, (2) preserved ancient subduction zone fabrics that generate an anisotropic fabric during accretion [*Yuan and Romanowicz*, 2010; *Wirth and Long*, 2014], (3) a global interface formed by the relaxation of the shear modulus and frequency-dependent attenuation from grain boundary sliding in the presence of hydrated phases [Karato 2012;

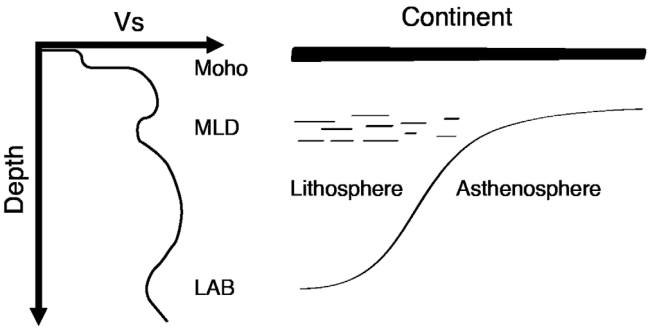

Figure 1. A schematic of a shear velocity profile (Vs) beneath a continent showing the inferred relative depths of a theoretical midlithospheric discontinuity (MLD) and the lithosphere-asthenosphere boundary (LAB).

Olugboji et al., 2013, *Karato*, 2014; *Karato et al*., 2015], (4) an abrupt change in the chemical composition of the lithospheric mantle, caused by metasomatism or crystallized melts [*Griffin et al*., 2009; *Savage and Silver*, 2008], or (5) an interface generated by melting induced by the gravitational collapse of continents in the Archean [*Rey et al*., 2014].

Most arguments for the presence of modern melt require high geothermal gradients that are inconsistent with the very low geothermal gradient expected in ancient cratons [e.g., *Jaupart and Mareschal*, 1999; *Michaut et al*., 2009; *Wölbern et al*., 2012], though the presence of relatively exotic melt compositions with low solidus temperatures, such as sulfidic melt [*Helffrich et al*., 2011] cannot be ruled out. The preservation of anisotropy (lattice-preferred orientation) associated with fabrics formed during ancient episodes of subduction has been proposed on the basis of xenolith textures [*Soustelle et al*., 2010]. However, it is difficult to ascertain from xenoliths alone if the anisotropy found at the hand sample scale would result in more broadly defined seismically observed anisotropy [*Fischer et al*., 2010]. The presence of a global interface associated with enhanced grain boundary sliding and indicative of mantle hydration state has also been proposed [*Karato*, 2012; *Olugboji et al*., 2013]; therefore interrogation of the hydration state of xenoliths will be a important test of this model. Here, we use the mineralogy and geochemistry of xenoliths originating from the depth of the MLD to evaluate a subset of current MLD-formation hypotheses, in particular the feasibility of crystallized melt and its ability to affect the chemical compositions and physical properties of the rock.

The hypothesis we explore in detail postulates that magma thermally equilibrates with surrounding rock and crystallizes where a geotherm crosses the solidus, forming a permeability barrier [e.g., *Sparks and Parmentier*, 1991]. One possible scenario is that the depth of the MLD is tied to the depth at which magma crosses the solidus. A component of this hypothesis is that partial melting will create a magma that is relatively rich in carbon and hydrogen compared to the dry, subsolidus surrounding peridotite [*Green et al*., 2014]. When this volatile-rich melt crystallizes, the resulting rocks bears hydrous or carbonate extra minerals that can significantly lower seismic wave speeds, either intrinsically [*Hacker et al*., 2003] or through mechanisms such as enhanced grain boundary sliding [*Olugboji et al*., 2013]. Xenoliths have been reported to contain carbon in the form of diamond, graphite, calcium carbonate, dolomite, and aragonite [*Ionov et al*., 1993; *Humphreys et al*., 2010; *Deines and Gold*, 1973; *Ionov et al*., 1996; *Lee et al*., 2000; *Duke*, 2009]. Carbonatite melts and associated silica-depleted igneous rocks are shown to have deep mantle sources [*Jones et al*., 2013; *Dasgupta and Hirschmann*, 2007; *Bailey*, 1990]. The solubility of water decreases in orthopyroxene to the point of exclusion around depths similar to the MLD, allowing for increase silicate melt production [*Mierdel et al*., 2007]. Furthermore, the presence of carbon-rich fluid in the mantle has also been inferred from xenoliths containing Na-rich amphiboles [*Yaxley et al*., 1998], Na-rich glasses [*Coltorti et al*., 1999], and major and trace element signatures of partial melting [*Lee and Wyllie*, 1997; *Aulbach et al*., 2013; *Chakhmouradian et al*., 2008]. Hydrous minerals, such as amphiboles and micas, also occur in xenoliths from the continental lithosphere all over the globe [e.g., *Yaxley et al*., 1998; *Lee and Wyllie*, 1997; *Lee et al*., 2000].

Our approach is to investigate the presence, and type of, infiltrated melt via trace element analyses of xenoliths [e.g., *McKenzie & O'nions*, 1991; *Michard*, 1989] and determine if these xenoliths have a depth association with the MLD. The MLD occurs across a depth interval that is well represented in the xenolith database, providing chemical observations to directly interrogate a compositional origin of the MLD. Experiments have shown that carbon-rich fluids increase key trace elements like U, Th, and Sr relative to high-field strength elements (HFSE) such as Zr, Hf, and Ti [*Green et al*., 1992; *Blundy and Dalton*, 2000; *Dasgupta et al*., 2009]. Increased U, Th, and Sr relative to Zr, Hf, and Ti in oceanic mantle xenoliths have been cited as evidence for interaction between peridotite and carbon-rich fluid at depths of 0.7–1.2 GPa [*Delpech et al*., 2004; *Coltorti et al*., 1999]. In continental arc settings, many xenoliths possess carbonatite signatures at depths of

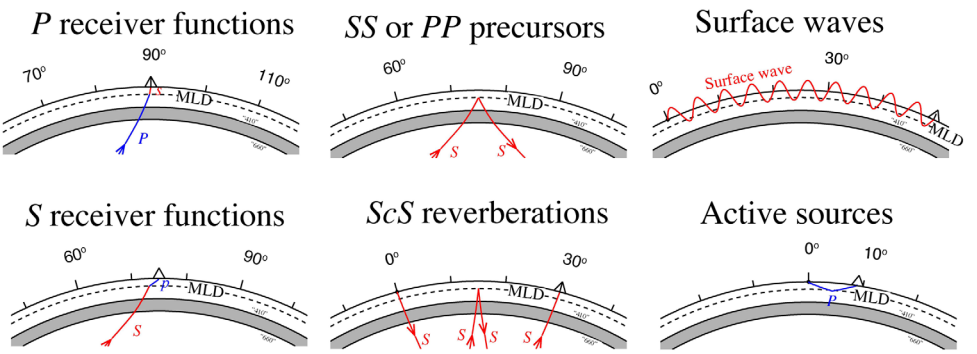

Figure 2. Representative ray paths for the seismic methods used to image the MLD. Arrows indicate direction of propagation from the seismic source to the receiver (triangle). Observations of the MLD from each phase are cataloged in the database in Table 1. Typical epicentral distances for each phase are indicated in degrees above each cross section.

0.9–1.8 GPa [*Ionov et al*., 1993]. Other mantle xenoliths from 1.5 to 2 GPa show trace element patterns indicative of cryptic carbonatite metasomatism [*Yaxley et al*., 1998]. Negative Ti-Zr-Hf anomalies in mantle xenoliths were identified in the Slave craton and attributed to the presence of carbon-rich melt above 145 km [*Aulbach et al*., 2013]. Thus there exists substantial evidence that crystallized volatile-rich melts are preserved in the continental midlithosphere near the expected depth of the MLD.

To investigate the expression of the MLD in continental mantle, we seek to clarify the uncertainty underlying the origin and evolution of the boundary by analyzing (1) a seismological database that collects a wide variety of observations across seismic methods and quantifies the regions where the MLD has been observed and characteristics of the observations (i.e., depth, % velocity decrease, and boundary width), (2) a petrological database of xenoliths that originate within (and not within) the depth range and vicinity of the observed seismological MLDs, and (3) thermodynamic modeling to assess the feasibility of the frozen-in melts for producing the observed petrological and seismological constraints.

2. Methods

2.1. The Seismological Database

Our database consists of seismological observations reported in the literature that detect a sharp seismic discontinuity in the midcontinental regions. We limited the search to observations within the depth range of 60–160 km, and to velocity decrease with depth to eliminate confusion with other seismic discontinuities, such as the Hales interface (a positive velocity contrast occurring at similar depth), the Gutenberg discontinuity (observed in oceanic mantle), and detections of the LAB [e.g., *Bodin et al*., 2014]. The MLD is thus defined in our study as occurring only beneath continental regions, though we readily acknowledge that the boundary may share many qualities of the Gutenberg discontinuity beneath the oceans, and may coincide with a discontinuity at the LAB beneath continental margins. We further attempt to distinguish detections of the MLD from a seismic discontinuity associated with the LAB by limiting our database to observations within cratonic lithosphere older than 1 Ga. Although some researchers propose very deep MLDs beneath South Africa [e.g., *Sodoudi et al*., 2013], we restrict our compilation to observations shallower than 160 km to avoid overlap with proposed LAB depths beneath cratonic regions from surface wave tomography [e.g., *Adams and Nyblade*, 2011; *Fishwick*, 2010; *Priestley et al*., 2008].

The MLD is detected by a wide variety of seismic methods (Figure 2): P to S receiver functions (Pds, conversion of an incoming P-wave to an S-wave), S to P receiver functions (Sdp, conversion of an incoming S-wave to a P-wave), SS and PP precursors (SdS, or PdP, underside reflections of S- or P-wave from a deep discontinuity halfway between a station and source), ScS reverberations (reverberation of S-wave energy that reflects from the core-mantle boundary prior to being reflected off of the MLD), decreases in shear velocity at midlithospheric depths from surface wave tomography that is sensitive to lithospheric and asthenospheric depths, and long-range, active-source seismic refraction experiments that identify scattering in the arrivals around distances of 8–14 degrees.

We compiled depth, location, and the approximate magnitude of the velocity decrease with depth across the discontinuity in different locations (Table 1). In some cases, authors do not report the extent of velocity

Table 1. MLD Observations Worldwide[a]

Reference	Method	Latitude	Longitude	Location	Depth	%ΔVs	Visual or Exact
North America							
Abt et al. [2010][b]	S-RF	50.25	−95.88	North America; ULM	101	n/a	Exact
		44.77	−79.14	North America; SADO	90	n/a	Exact
		38.23	−86.29	North America; WCI	97	n/a	Exact
		36.13	−87.83	North America; WVT	113	n/a	Exact
		44.57	−74.98	North America; PTN	69	n/a	Exact
		39.1719	−86.5222	North America; BLO	111	n/a	Exact
		34.98	−88.08	North America; PLAL	83	n/a	Exact
		42.2997	−83.6561	North America; AAM	90	n/a	Exact
		37.2113	−80.421	North America; BLA	69	n/a	Exact
		35.89	−79.09	North America; CEH	99	n/a	Exact
		47.9462	−91.495	North America; EYMN	94	n/a	Exact
		42.9148	−90.2488	North America; JFWS	59	n/a	Exact
		33.03	−87	North America; LRAL	91	n/a	Exact
		39.6581	−79.8456	North America; MCWV	91	n/a	Exact
Courtier and Revenaugh [2006]	ScS Reverb.	28.755	−79.128	Eastern United States	123	−13.76	
Darbyshire et al. [2013]	Surface wave	62–66	−75 to −90	Northern Hudson Bay	∼90	−5 to 8%	Visual
Foster et al. [2014][b]	S-RF and SKS-RF	36–48	−97 to −91	American Midwest	87	n/a	Exact
Hansen et al. [2013][b]	S-RF and SKS-RF	36–40	−108 to −104	Colorado Rockies	70–100	n/a	Visual
Hopper et al. [2014][b]	S-RF	46	−107 to −106	Wyoming Craton	70–75	n/a	Visual
		44	−108 to −104	Wyoming Craton	78–85	n/a	Visual
		41	−111 to −110	Wyoming Craton	63–72	n/a	Visual
		45–46	−107 to −110	Wyoming Craton	70–80	n/a	Visual
Kind et al. [2015]	S-RF	34–47	−82 to −102	Northern U.S.	95–115	n/a	Visual
Kumar et al. [2005a,b][b]	S-RF	72	−55	Greenland	110	n/a	*Kind et al.* [2012]
		64	−53	Greenland	110	n/a	*Kind et al.* [2012]
		75	−42	Greenland	80	n/a	*Kind et al.* [2012]
		69	−45	Greenland	100	n/a	*Kind et al.* [2012]
		68	−28	Greenland	70	n/a	*Kind et al.* [2012]
		65	−36	Greenland	80	n/a	*Kind et al.* [2012]
		83	−60	Greenland	70	n/a	*Kind et al.* [2012]
		80	−60	Greenland	100	n/a	*Kind et al.* [2012]
Kumar et al. [2012]	S-RF	29–51	−115 to −75	U.S. Array	51–135	n/a	Exact
Lekic and Fischer [2014][b]	S-RF	38.5–35.5	−112 to −107.5	Colorado Plateau	70–90	−3%	Visual
		41.5	−111 to −107	Wyoming Craton	70–90	−3%	Visual
Miller and Eaton [2010]	S-RF	54.725	−101.9783	North America; FFC	∼150	n/a	Visual
		58.7616	−94.0866	North America; FCC	∼110	n/a	Visual
		62.4183	−77.9113	North America; IVKQ	∼100	n/a	Visual
		63.7469	−68.5451	North America; FRB	∼130	n/a	Visual
Porritt et al. [2015]	S-RF and SKS-RF	50–72	−98 to −65	Hudson Bay	80–120	n/a	Visual
Rychert et al. [2005][b]	P-RF	42.51	−71.56	North America; HRV	61	n/a	Exact
Rychert and Shearer [2009]	P-RF; distinct from mults.	47.946	−91.495	North America; EYMN	95	n/a	Exact
		54.725	−101.9783	North America; FFC	89	n/a	Exact
		63.747	−68.545	North America; FRB	134	n/a	Exact
		63.747	−68.545	North America; FRB	77	n/a	Exact
Snyder [2008]	P-RF						
Thybo [2006]	Refraction	63–66	−114 to −109	Northwestern Canada	145	n/a	Visual
	Profile1						
	Profile2a	[38 32 34]	[−122 −102 −86]		∼100		Visual
	Profile2b	[61 34]	[−98 −78]		∼100		Visual
	Profile2c	[64 54]	[−117 −98]		∼100		Visual
	Profile2d	[60 53 47 48 54]	[−137 −121 −90 −75 −66]		∼100		Visual
	Profile2e	[47 43]	[−75 −65]		∼100		Visual
	Profile2f	[45 46]	[−118 −91]		∼100		Visual
	Profile2g	[35 38 46]	[−116 −103 −90]		∼100		Visual
	Profile2h	[32 46]	[−100 −90]		∼100		Visual
	Profile3	[33 45]	[−92 −89]		∼100		Visual
	Profile4	[50 38]	[−120 −120]		∼100		Visual
	Profile5	[27 15]	[−110 −85]		∼100		Visual
	Profile6	[36 30]	[−118 −116]		∼100		Visual
	Profile7	[51 29]	[−124 −115]		∼100		Visual
Wirth and Long [2014][b]	P-RF; transverse and radial	[59 32]	[−110 −109]		∼100		Visual
		36.13	−87.83	North America; WVT	101.5	n/a	Exact
		38.23	−86.29	North America; WCI	86.5	n/a	Exact
		39.1719	−86.5222	North America; BLO	86.5	n/a	Exact
Yuan et al. [2006][b]	S-RF	38.056	−91.245	North America; CCM	78.5	n/a	Exact
Zheng and Romanowicz [2012]	S660S double precursors	62.56	−114.61	Slave Craton; YKW3	120	n/a	Exact
					125		

Table 1. (continued)

Reference	Method	Latitude	Longitude	Location	Depth	%ΔVs	Visual or Exact
Europe/Asia							
Bodin et al. [2014][b]	Cnvrtd phases + dispersion	17.417	78.55	Indian Shield; HYB	110	−5	Exact
Geissler et al. [2010][b]	S-RF	49.631	22.708	Poland; KWP	129	−5	Exact
		54.958	37.767	Russia; MHV	102	−5	Exact
		55.685	12.433	Denmark; COP	125	−5	Exact
		59.649	9.598	Norway; KONO	116	−5	Exact
Heit et al. [2010]	SS precursor			Tibet/China			
Kind et al. [2013]	S-RF	[57 71]	[13 32]	Scandanavia	100	n/a	Visual
Kumar et al. [2005a,b]	S-RF	45	77	Tienshan, China	120	n/a	*Kind et al.* [2012]
		44	77	Tienshan, China	100	n/a	*Kind et al.* [2012]
		43	77	Tienshan, China	120	n/a	*Kind et al.* [2012]
		33	77	Karakoram, China	120	n/a	*Kind et al.* [2012]
Kumar et al. [2007]	S-RF	17.42	78.55	India; HYB	101	n/a	Exact
		23.52	45.5	Saudi Arabia; RAYN	138	n/a	Exact
Revenaugh and Sipkin [1995]	ScS Reverb.	31.819	86.509	**China**	158	−8.6	
			37.148	87.1198	China	145	−6.2
			40.506	78.8797	China	131	−9.2
			46.952	114.12911	China	133	−2.4
			46.424	131.372	China	84	−4.2
			49.915	133.35605	China	80	−5.6
			39.563	115.045	China	79	−6
			35.66	127.099	China	64	−12
			42.026	130.849	China	72	−7.6
			36.537	122.618	China	123	−4.2
			40.636	121.856	China	103	−7.8
			46.125	127.191	China	147	−4.4
Rychert and Shearer [2009]	P-RF; distinct from mults.	17.417	78.55	Indian Shield; HYB	65	n/a	Exact
Saul et al. [2000]	P-RF	17.417	78.55	Indian Shield; HYB	90	n/a	Exact
Sodoudi et al. [2006][b]	S-RF	29–32	114.5–117	China; Yangtze Craton	72	n/a	Visual
		32–34.5	114.5–117	China; North China Platform	60	n/a	Visual
Tonegawa and Helffrich [2012]	sS precursors			Phillipine Sea Plate	59.3	−5.8	
Zhang and Lay [1993]				N Korea (weak MLD)	90	−11.4	
				Sea of Okhotsk (weak MLD)		−11.4	
				Izu Japan	66	−12.6	
Thybo [2006]	Refraction						
	Profile8a	[71 61]	[26 19]		∼100		Visual
	Profile8b	[59 52]	[17 13]		∼100		Visual
	Profile9	[65 53]	[23 18]		∼100		Visual
	Profile10	[47 42]	[−8 8]		∼100		Visual
	Profile11a	[49 35]	[−1 22]		∼100		Visual
	Profile11b	[50 38]	[3 25]		∼100		Visual
	Profile12a	[29 51]	[−1 17]		∼100		Visual
	Profile12b	[34 52]	[−8 14]		∼100		Visual
	Profile13a	[55 57 43]	[−1 32 73]		∼100		Visual
	Profile13b	[50 68 74]	[−7 22 56]		∼100		Visual
	Profile14	[70 64 49]	[42 71 95]		∼100		Visual
	Profile15	[57 65 56]	[62 104 138]		∼100		Visual
	Profile16	[65 73 65]	[61 104 143]		∼100		Visual
	Profile17	[75 63 50]	[82 93 101]		∼100		Visual
	Profile18	[76 53]	[95 116]		∼100		Visual
South America							
Heit et al. [2007]	S-RF; SKS-RF	5.11	−52.64	French Guyana; MPG	70	n/a	Exact
		−5.82	−35.9	NE Brazil; RCBR	80	n/a	Exact
		−26.33	−57.33	Paraguay; CPUP	80	n/a	Exact
		−8.94	−63.18	Amazonas; SAML	130	n/a	Exact
		−15 to −15.64	−49 to −48.01	Central Brazil	140	n/a	Exact
		−22	−52	Parana Basin	120	n/a	Exact
		−23 to −23.52	−45 to −47.43	Brazilian Coast	80	n/a	Exact
		−38.05	−61.97	Central Argentina; TRQA	120	n/a	Exact
Rychert and Shearer [2009]	P-RF; distinct from mults.	−23.593	−47.427	Brazil; SPB	80	n/a	Exact
Africa							
Hansen et al. [2009][b]	S-RF	−26 to −31	21–32	South Africa	160	−4.5	Visual
Kumar et al. [2007]	S-RF	−19.2	17.58	Namibia; TSUM	127	n/a	Exact
		−32.38	20.81	South Africa; SUR	134	n/a	Exact
		−28.61	25.26	South Africa; BOSA	150	n/a	Visual
		−15.28	28.19	Zambia; LSZ	150	n/a	Visual
		−25.02	25.6	Botswana; LBTB	150	n/a	Visual
Rychert and Shearer [2009]	P-RF; distinct from mults.	−25.015	25.597	Botswana; LBTB	88	n/a	Exact
		−28.614	25.256	South Africa; BOSA	96	n/a	Exact

Table 1. (continued)

Reference	Method	Latitude	Longitude	Location	Depth	%ΔVs	Visual or Exact
		22.791	5.528	Algeria; TAM	100	n/a	Exact
		22.791	5.528	Algeria; TAM	73	n/a	Exact
Savage and Silver [2008][b]	S-RF; P-RF	−19 to −30	23–31	South Africa	150	−4.5	Visual
Sodoudi et al. [2013][b]	S-RF	−33 to −20	19.5–32	South Africa	77–97	3% anisotropy	Visual
		−32 to −19	20.6–32.9	South Africa	140–192	n/a	Visual
Wittlinger and Farra [2007]	S-RF; SKS-RF; P-RF	−19 to −33	22–30	South Africa	70–151	−5	Visual
Wolbern et al. [2013][b]	S-RF; SKS-RF	−2 to 1	29–33	Tanzania Craton; Albertine	60–100	−12 to −24	Visual
Australia							
Ford et al. [2010][b]	S-RF; P-RF	−18.1	125.64	FITZ	81	n/a	Exact
		−30.78	128.06	FORT	79	n/a	Exact
		−31.37	121.88	KMBL	85	n/a	Exact
		−19.93	134.36	WRAB	81	n/a	Exact
		−21.16	119.73	MBWA	69	n/a	Exact
		−32.93	117.24	NWAO	81	n/a	Exact
Thybo [2006]	Refraction						
	Profile19a	[−9 −22]	[113 135]		∼100		Visual
	Profile19b	[2 −21]	[129 138]		∼100		Visual
Antarctica							
Heeszel et al. [2013]	Surface wave	−85 to −78	60–100	Gamburtsev Mtns	75	−2	Visual

[a]Latitude, longitude, and depth are denoted as: (a) Exact values reported by the authors or (b) visually identified approximate values.
[b]Indicates receiver function studies that include higher frequencies (>4 s for SRF; >1 s for PRF).

decrease (N/A in Table 1). We take into consideration the resolutions of the different methods, both laterally and with depth. For example, S receiver functions will average over a larger area than P receiver functions. Alternatively, a MLD signal in the P receiver function, if not processed carefully, can be obscured by crustal reverberations [*Rychert et al*., 2010]. Although S-wave receiver function methods have been compiled and discussed in recent work from *Selway et al*. [2015], our compilation expands upon this by including receiver function observations (both Sp and Ps), and encompasses observations from other seismic methods. In subsequent sections, we discuss pertinent details of each detection method and how they can affect observations interpreted as an MLD.

2.2. Geochemistry and Petrology of Xenoliths

The geochemical database PetDB [*Lehnert et al*., 2000] was systematically searched for compositional information on xenoliths found within continental areas. To test our hypothesis regarding the occurrence of crystallized melts, we used search criteria that included xenoliths with depth information that hosted amphibole, phlogopite, carbonate minerals, graphite (Table 2), and published trace element concentrations (Table 3). Depths were either published in the database and calculated using the two-pyroxene method of *Brey and Köhler* [1990], or were assigned the depth range based on the stability of spinel lherzolite of 0.9–1.8 Gpa [*Demény et al*., 2004; *Ionov et al*., 1996; *Delpech et al*., 2004]. We also report on xenoliths from tectonic settings and depths of the mantle where the MLD is not predicted to exist by our hypothesis (e.g., very deep below young lithosphere, for example) as a comparison to further test our hypothesis. Trace-element analyses of carbonatites and hydrous minerals are collected also from PetDB by searching for individual analyses of CARB, CC, AMPH, and PHLOG that had trace element data. This data set includes material irrespective of tectonic setting or depth, as not many analyses existed within PetDB.

3. Seismological Results

We compiled seismological results from six methodologies to determine where the MLD has been detected. These results are summarized in Table 1. A useful outcome of this compilation is that we are able to readily identify regions with either a paucity or abundance of observations, indicating where future research targets for investigating the evolution of cratonic lithosphere may be most beneficial.

3.1. Active Source Seismology

Active source seismic surveys provide a spatially high-resolution approach for studying lithospheric structures. A global compilation of high-density seismic refraction experiments that sample the continental lithosphere at long ranges (300–2500 km) reveals the existence of strong scattering beyond the 700–900-km

Table 2. Mineralogy of Xenoliths

Sample Name	Source	Latitude	Longitude	Minerals	Depth (Gpa)	Temperature (°C)	Geologic Setting	Xenolith Type
MUKHSIE-BC-F-68[c]	*Mukhopadhyay and Manton* [1994]	37.21	−119.26	Amph, Phlog	1.1	674	Convergent margin	Pyroxenite
LOOGERM-EE-S1[c]	*Loock et al.* [1990]	50.17	6.85	Amph	0.2	721	Intraplate, off-craton	Granulite
LOOGERM-WE-S35[c]	*Loock et al.* [1990]	50.17	6.85	Amph	0.2	655	Intraplate, off-craton	Granulite
LOOGERM-EE-S12	*Loock et al.* [1990]	50.17	6.85	Amph	0.8	737	Intraplate, off-craton	Granulite
FRANAK-NUN-13004[c]	*Francis* [1976]	60	−166.5	Amph	0.9	964	Intraplate, off-craton	Pyroxenite
ARCAUST-LB-83-2[c]	*Arculus et al.* [1988]	−38.2	143.1	Amph	0.9	881	Intraplate, off-craton	Pyroxenite
LOOGERM-WE-S16[c]	*Loock et al.* [1990]	50.17	6.85	Amph	1.0	864	Intraplate, off-craton	Granulite
LOOGERM-WE-S37[c]	*Loock et al.* [1990]	50.17	6.85	Amph	1.1	853	Intraplate, off-craton	Granulite
LOOGERM-EE-S1[c]	*Loock et al.* [1990]	50.17	6.85	Amph	1.2	816	Intraplate, off-craton	Granulite
MUKHSIE-PSM-PS20[c]	*Mukhopadhyay and Manton* [1994]	37.21	−119.26	Amph	1.5	780	Convergent margin	Pyroxenite
KEMRUSS-KOLA-436-17[c]	*Kempton et al.* [1995]	67	32.5	Amph	1.6	738	Intraplate, craton	Granulite
LOOGERM-WE-S35[c]	*Loock et al.* [1990]	50.17	6.85	Amph	1.6	791	Intraplate, off-craton	Granulite
LOOGERM-WE-S37[c]	*Loock et al.* [1990]	50.17	6.85	Amph	1.6	883	Intraplate, off-craton	Granulite
LOOGERM-WE-S16[c]	*Loock et al.* [1990]	50.17	6.85	Amph	1.6	902	Intraplate, off-craton	Granulite
FRANAK-NUN-14001[c]	*Francis* [1976]	60	−166.5	Amph	1.8	1080	Intraplate, off-craton	Pyroxenite
LITRUSS-VIT-V462[c]	*Litasov et al.* [2000]	53.5	113.1	Amph	2.2	1112	Continental rift	Peridotite
JANSLOV-POH-119-5[c]	*Janak et al.* [2006]	46.4	15.5	Amph	2.5	918	Intraplate, off-craton	Peridotite
IONRUSS-VIT-313-103[c]	*Ionov et al.* [1993]	59.45	112.55	Amph	2.6	1105	Continental rift	Peridotite
JANSLOV-POH-119-5[c]	*Janak et al.* [2006]	46.4	15.5	Amph	2.9	770	Intraplate, off-craton	Peridotite
JANSLOV-POH-VI01/04[c]	*Janak et al.* [2006]	46.4	15.5	Amph	3.5	1128	Intraplate, off-craton	Peridotite
MUKHSIE-PSM-PS20[c]	*Mukhopadhyay and Manton* [1994]	37.25	−119.33	Amph	6.0	1209	Convergent margin	Pyroxenite
DANCSAF-RVD175[c]	*Danchin* [1979]	−25.6593	28.5078	Phlog	1.1	681	Intraplate, craton	Peridotite
DANCSAF-RVD500[c]	*Danchin* [1979]	−25.6593	28.5078	Phlog	2.0	1097	Intraplate, craton	Peridotite
DANCSAF-RVD501[c]	*Danchin* [1979]	−25.6593	28.5078	Phlog	2.0	1072	Intraplate, craton	Peridotite
EHRECOL-THUMB-121[c]	*Ehrenberg* [1982]	36.6	−109.05	Phlog	2.1	1075	Intraplate, off-craton	Peridotite
EHRECOL-THUMB-B712[c]	*Ehrenberg* [1982]	36.6	−109.05	Phlog	2.3	1109	Intraplate, off-craton	Pyroxenite
EHRECOL-THUMB-F077[c]	*Ehrenberg* [1982]	36.6	−109.05	Phlog	2.3	1203	Intraplate, off-craton	Peridotite
EHRECOL-THUMB-H077[c]	*Ehrenberg* [1982]	36.6	−109.05	Phlog	2.4	1157	Intraplate, off-craton	Peridotite
GLASRUS-VIT-SG96B13[c]	*Glaser et al.* [1999]	59.5	112.5	Phlog	2.5	1161	Continental rift	Peridotite
IONRUSS-VIT-313-110[c]	*Ionov et al.* [1993]	59.45	112.55	Phlog	2.9	1265	Continental rift	Peridotite
IONRUSS-VIT-313-7[c]	*Ionov et al.* [1993]	59.45	112.55	Phlog	3.0	805	Continental rift	Peridotite
IONRUSS-VIT-314-74[c]	*Ionov et al.* [1993]	59.45	112.55	Phlog	3.1	830	Continental rift	Peridotite
LEETANZ-001-LB34[c]	*Lee and Rudnick* [1999]	−3.6	36.75	Phlog	3.2	1116	continental rift	Peridotite
LITRUSS-VIT-V202[c]	*Litasov et al.* [2000]	53.5	113.1	Phlog	3.5	914	Continental rift	Pyroxenite
LITRUSS-VIT-V439[c]	*Litasov et al.* [2000]	53.5	113.1	Phlog	4.0	1090	continental rift	Peridotite
LITRUSS-VIT-V462[c]	*Litasov et al.* [2000]	53.5	113.1	Phlog	4.0	1023	continental rift	Peridotite
LITRUSS-VIT-V857[c]	*Litasov et al.* [2000]	53.5	113.1	Phlog	4.1	1253	Continental rift	Peridotite
MUKHSIE-BC-F-51[c]	*Mukhopadhyay and Manton* [1994]	37.21	−119.26	Phlog	4.2	1159	Convergent margin	Pyroxenite
REHFSAF-DJ0216[c]	*Rehfeldt et al.* [2008]	−28	24.5	Phlog	4.4	1125	Intraplate, craton	Peridotite
REHFSAF-DJ0217[c]	*Rehfeldt et al.* [2008]	−28	24.5	Phlog	4.4	1064	Intraplate, craton	Peridotite
REHFSAF-DJ0218[c]	*Rehfeldt et al.* [2008]	−28	24.5	Phlog	4.5	1215	Intraplate, craton	Peridotite
REHFSAF-DJ0256F[c]	*Rehfeldt et al.* [2008]	−28	24.5	Phlog	4.7	1207	Intraplate, craton	Peridotite
RUDTANZ-089-664[c]	*Rudnick et al.* [1994]	−3.4	36.43	Phlog	4.8	1191	Continental rift	Peridotite
RUDTANZ-089-664[c]	*Rudnick et al.* [1994]	−3.4	36.43	Phlog	5.2	1263	continental rift	Peridotite
RUDTANZ-089-674[c]	*Rudnick et al.* [1994]	−3.4	36.43	Phlog	6.5	1414	continental rift	Peridotite
BALIHUN-SZEN-SZB21[b]	*Bali et al.* [2008]	46.8	17.3	Calcium carbonate	1.6	953	Intraplate, off-craton	Peridotite
BALIHUN-SZEN-SZB50[b]	*Bali et al.* [2008]	46.8	17.3	Calcium carbonate	1.5	815	Intraplate, off-craton	Pyroxenite
BALIHUN-SZEN-SZB55[b]	*Bali et al.* [2008]	46.8	17.3	Calcium carbonate	1.9	913	Intraplate, off-craton	Peridotite
BALIHUN-SZEN-SZB59[b]	*Bali et al.* [2008]	46.8	17.3	Calcium carbonate	2	1014	Intraplate, off-craton	Peridotite
CVETSRB-PNB-M/SB2[c]	*Cvetkovic et al.* [2007]	45	19	Calcium carbonate	0.9–1.8	N/A	Intraplate, off-craton	Peridotite
CVETSRB-PNB-M/SB6[c]	*Cvetkovic et al.* [2007]	45	19	Calcium carbonate	0.9–1.8	N/A	Intraplate, off-craton	Peridotite
DELPKER-LM/BY96-357[c]	*Delpech et al.* [2004]	−49.5	60.5	Calcium carbonate	0.9–1.8	N/A	Intraplate, off-craton	Peridotite
DELPKER-LM/BY96-381[c]	*Delpech et al.* [2004]	−49.5	60.5	Calcium carbonate	0.9–1.8	N/A	Intraplate, off-craton	Peridotite
DEMHUN-001-SZT-1111c	*Demény* [2004]	47.1	17.9	Calcium carbonate	0.9–1.8	N/A	Intraplate, off-craton	Peridotite
DEMHUN-001-SZT-1130[c]	*Demény* [2004]	47.1	17.9	Calcium carbonate	0.9–1.8	N/A	Intraplate, off-craton	Peridotite
IOSPTSB-21-5[c]	*Ionov et al.* [1996]	78.93	11.93	Calcium carbonate	0.9–1.8	910	Intraplate, off-craton	Peridotite
IOSPTSB-21-5[c]	*Ionov et al.* [1996]	78.93	11.93	Calcium carbonate	0.9–1.8	910	Intraplate, off-craton	Peridotite
IOSPTSB-21-6[c]	*Ionov et al.* [1996]	78.93	11.93	Calcium carbonate	0.9–1.8	930	Intraplate, off-craton	Peridotite
IOSPTSB-315-6[c]	*Ionov et al.* [1996]	78.93	11.93	Dolomite	0.9–1.8	860	Intraplate, off-craton	Peridotite
IOSPTSB-318[c]	*Ionov et al.* [1996]	78.93	11.93	Dolomite	0.9–1.8	900	Intraplate, off-craton	Peridotite
IOSPTSB-4-24-90[c]	*Ionov et al.* [1996]	78.93	11.93	Dolomite	0.9–1.8	980	Intraplate, off-craton	Peridotite
IOSPTSB-4-36-90[c]	*Ionov et al.* [1996]	78.93	11.93	Dolomite	0.9–1.8	940	Intraplate, off-craton	Peridotite
IOSPTSB-4-90-9[c]	*Ionov et al.* [1996]	78.93	11.93	Calcium carbonate	0.9–1.8	980	Intraplate, off-craton	Peridotite
IOSPTSB-43-86[c]	*Ionov et al.* [1996]	78.93	11.93	Dolomite	0.9–1.8	920	Intraplate, off-craton	Peridotite
IOSPTSB-63-90-18[c]	*Ionov et al.* [1996]	78.93	11.93	Calcium carbonate	0.9–1.8	870	Intraplate, off-craton	Peridotite
LEETANZ-001-LB19-C[c]	*Lee et al.* [2000]	−4.5	35.4	Calcium carbonate	0.9–1.8	N/A	Continental rift	Peridotite
LEETANZ-001-LB58[c]	*Lee et al.* [2000]	−4.5	35.4	Calcium carbonate	0.9–1.8	N/A	Continental rift	Peridotite

Table 2. (continued)

Sample Name	Source	Latitude	Longitude	Minerals	Depth (Gpa)	Temperature (°C)	Geologic Setting	Xenolith Type
LEETANZ-001-MON-CARB[c]	*Lee et al.* [2000]	−3.25	36.48	Calcium carbonate	0.9–1.8	N/A	Continental rift	Peridotite
LEETANZ-001-PEL2[c]	*Lee et al.* [2000]	−3.75	37.75	Calcium carbonate	0.9–1.8	N/A	Continental rift	Peridotite
LUCARG-CNCH-4-227[c]	*Lucassen et al.* [2005]	−26	−65.75	Calcium carbonate	0.9–1.8	N/A	Continental rift	Peridotite
LUCARG-CNCH-4-229[c]	*Lucassen et al.* [2005]	−26	−65.75	Calcium carbonate	0.9–1.8	N/A	Continental rift	Peridotite
LUCARG-CNCH-4-301A[c]	*Lucassen et al.* [2005]	−26	−65.75	Calcium carbonate	0.9–1.8	N/A	Continental rift	Peridotite
LUCARG-CNCH-A-113E[c]	*Lucassen et al.* [2005]	−26	−65.75	Calcium carbonate	0.9–1.8	N/A	Continental rift	Peridotite
LUCARG-CNCH-A57-1[c]	*Lucassen et al.* [2005]	−26	−65.75	Calcium carbonate	0.9–1.8	N/A	Continental rift	Peridotite
SON0166-G035-014[c]	*Franz and Romer* [2010]	−3.5	152.5	Calcium carbonate	0.9–1.8	N/A	Convergent margin	Peridotite

[a]Depth calculated from *Brey and Köhler* [1990].
[b]Depth reported in PetDB.
[c]Depth limited by spinel.

offset, called the "8° Discontinuity" [*Thybo and Perchuc*, 1997]. The 8° Discontinuity has been proposed to be a low-velocity zone (LVZ) below depths of 100 km [*Thybo and Perchuc*, 1997; *Chu et al*., 2012], within the defined search criterion for the depth of the MLD. *Thybo and Perchuc* [1997] modeled these LVZ scatterers with fine-layered (40 km-thick) structures, which can extend to depths of about 180 km in "cold" regions and about 400 km in "hot" regions.

3.2. Surface Waves

Surface wave tomography probes the three-dimensional absolute shear wave velocity structure within the deep earth. Surface waves are dispersive, and the phase velocities of different frequency bands are sensitive to structures at different depths. Global surface-wave tomography studies reveal a low isotropic shear wave velocity zone (LVZ) beneath oceans, with a top that falls at greater depth with plate age [*Nettles and Dziewoński*, 2008; *Maggi et al*., 2006; *Beghein et al*., 2014]. While the depth and the existence of the low-velocity zone beneath cratonic regions remains under debate, surface wave studies image an intralithospheric low-velocity layer at ∼100 km depth beneath continental cratons [e.g., *Cammarano and Romanowicz*, 2007]. The shear-wave velocity profile reveals that a transition from a fast seismic lid to a deeper slower zone coincides spatially with negative discontinuities found using receiver functions [*Cammarano and Romanowicz*, 2007]. Various regional studies have identified the MLD, although the depth varies within different cratons (Table 1). Also, vertical variations in velocity and azimuthal anisotropy from surface-wave tomography indicate that a change in seismic anisotropy coincides with the middle lithosphere low velocity layer [*Yuan and Romanowicz*, 2010; *Darbyshire et al*, 2013]. Surface waves are insensitive to sharp velocity jumps, thus it is desirable to compare surface-wave velocity models with those from other techniques.

3.3. Receiver Functions

Receiver functions (Pds and Sdp conversions) are used to identify the relatively sharp changes in seismic velocity with depth associated with mantle discontinuities. They have relatively high spatial resolution, sampling shallow upper mantle structures within ∼50 km laterally from the station for Pds and ∼500 km for Sdp [*Rychert et al*., 2010; *Kind et al*., 2012]. Earthquakes at epicentral distances of 30°–90° and 55°–85° are used for P and S receiver function analysis, respectively [e.g., *Abt et al*., 2010; *Kind et al*., 2012]. Pds or Sdp phases are used to explore lithospheric structure, although SKSdp may also be useful [*Kind et al*., 2012]. Studies that inspect multiple phases and dominant frequencies can help resolve the gradient across the discontinuity. P-receiver functions are able to detect fine structures of the lithosphere due to their high-frequency content, but Pds conversions from the MLD can be contaminated by crustal reverberations [*Rychert et al*., 2010]. On the other hand, S-receiver functions are free from reverberations due to shallow structures, but their low-frequency content limits the lateral and vertical resolution of the MLDs. Changes in azimuthal anisotropy with depth can be obtained from receiver functions where incoming seismic energy comes in to a seismometer from all backazimuths [e.g., *Levin and Park*, 1997; Savage, 1998; *Sodoudi et al*, 2013; *Wirth and Long*, 2014]. Given the limited occurrence of usable earthquakes (i.e., distance, depth, magnitude), however, identification of changes in anisotropy with depth is not feasible in all regions.

Several Sdp and Pds studies have identified a sharp boundary from ∼60 to 160 km deep at many locations [e.g., *Fischer et al*., 2010 and refs. therein; *Rychert et al*., 2010 and references therein; *Kind et al*., 2012 and

Table 3. Trace Element Data for Xenoliths

Sample Name	Source	Latitude	Longitude	Pressure (Gpa)	MLD (GPa)	LAB (Gpa)	Geologic Setting	Xenolith Type	La	Ce	Nd	Sm	Eu	Tb	Dy	Ho	Er	Tm	Yb	Lu	Ba	Cr	Hf	Nb	Ni	Rb	Sc	Sr	Ta	V	Y	Zr	Th	U
Depleted Mantle	*Workman and Hart* [2005]	N/A	N/A	N/A	N/A	N/A	N/A		0.192	0.55	0.581	0.239	0.096	0.07	0.505	0.115	0.348	0.505	0.365	0.058	0.563		0.157	0.15		0.05		7.664	0.01		3.33	5.08	0.0079	0.0032
Non-MLX																																		
CARWYO-WK-H68-16B	*Dawson* [1999]	−4.5671	35.4313	3.1	N/A		Continental rift	Peridotite	2.157	4.212	1.595	0.286	0.078	0.024	0.082	0.01	0.029		0.019	0.001	67.4		0.15	5.25	2128	10	11.6	33.6		46.7	0.45	5.39		
IONRUSS-VIT-313-105	*Ionov et al.* [2005]	59.45	112.55	2.1	N/A		continental rift	Peridotite													260	2547		1	2462	9.6	3.6	51.4		36.8	0.9	13		
IONRUSS-VIT-313-110	*Ionov et al.* [2005]	59.45	112.55	2.1	N/A		continental rift	Peridotite	0.477	1.165	0.572	0.197	0.065	0.032	0.167	0.026	0.073		0.047	0.004	29.8		0.126	0.94	2168	2.1	12.4	19.2		42.5	0.51	5		
IONRUSS-VIT-313-54	*Ionov et al.* [2005]	59.45	112.55	2.3	N/A		Continental rift	Peridotite	0.706	1.791	0.817	0.157	0.041	0.012	0.027	0.002	0.009		0.011	0.002	28		0.078	1.15	2319	2.2	11.1	29.6		39.1		2.87		
IONRUSS-VIT-314-56	*Ionov et al.* [2005]	59.45	112.55	1.5	N/A		Continental rift	Peridotite	1.683	3.311	1.376	0.287	0.083	0.024	0.117	0.016	0.053		0.033	0.001	186.7		0.206	4.97	2125	25.7	7.9	49.4		38.7	0.27	7.49		
IONRUSS-VIT-314-58	*Ionov et al.* [2005]	59.45	112.55	1.5	N/A		Continental rift	Peridotite	0.539	1.263	0.572	0.163	0.05	0.02	0.091	0.013	0.041		0.034	0.001	69.9		0.132	1.02	2296	3.4	10.6	43.2		56.8	0.16	5.14		
IONRUSS-VIT-314-59	*Ionov et al.* [2005]	59.45	112.55	1.8	N/A		Continental rift	Peridotite	0.43	1.47	1.62	0.63	0.25	0.16		0.24	0.72		0.78	0.12	0.05		0.39	0.02		0.01		16.35	0.01		6.16	13.7	0.02	0.02
IONRUSS-VIT-314-74	*Ionov et al.* [2005]	59.45	112.55	2.0	N/A		Continental rift	Peridotite	0.41	1.04	0.83	0.28	0.12	0.078		0.12	0.34	0.05	0.33	0.055	5.4		0.198	0.6		0.16		14.9	0.03			6.32	0.034	0.02
PETDB-1917-X-B	*Schilling et al.* [2005]	−49.1167	−70.1333	1.6	N/A		Convergent margin	Peridotite	0.77	1.67	1.07	0.33	0.13	0.086		0.15	0.49	0.079	0.55	0.099	4.6		0.205	0.91		0.22		24.5	0.05			7	0.075	0.06
PETDB-1917-X-C	*Schilling et al.* [2005]	−49.1167	−70.1333	1.6	N/A		Convergent margin	Peridotite	0.55	1.35	0.99	0.34	0.13	0.09		0.14	0.4	0.061	0.4	0.065	6		0.216	0.82		0.3		18.6	0			7.22	0.046	0.02
PETDB-1917-X-D	*Schilling et al.* [2005]	−49.1167	−70.1333	2.1	N/A		Convergent margin	Peridotite	0.65	1.43	1.17	0.39	0.16	0.104		0.16	0.45	0.067	0.44	0.071	7.3		0.271	0.72		0.2		20.5	0.04			9	0.051	0.02
PETDB-1917-X-F	*Schilling et al.* [2005]	−49.1167	−70.1333	3.6	N/A		Convergent margin	Peridotite	0.26	0.68	0.72	0.28	0.12	0.081		0.13	0.38	0.057	0.37	0.062	15.8		0.195	0.44		0.15		15.3	0.01			6.15	0.02	0.01
PETDB-1917-X-G	*Schilling et al.* [2005]	−49.1167	−70.1333	2.1	N/A		Convergent margin	Peridotite	0.64	1.56	1.07	0.32	0.12	0.075		0.11	0.31	0.047	0.3	0.05	4		0.189	0.78		0.22		16.6	0.04			6.03	0.069	0.03
MUKHSIE-PSM-PS11	*Mukhopadhyay and Manton* [1994]	37.25	−119	2.7	N/A	1.6–2.1	Convergent Margin	Pyroxenite	0.76	1.26	0.8	0.2	0.07	0.044		0.06	0.18	0.027	0.18	0.03	25		0.116	1.01		0.24		16.3	0.05			4.04	0.059	0.02
CARWYO-WK-H68-16B	*Carlson et al.* [1999]	47.07	−109.43	4.6	2.98–3.3	4–7.2	Intraplate craton	Peridotite	0.657	0.308	0.75	0.236	0.138	0.065		0.098	0.295	0.04	0.264	0.042	5.5			0.08		0.32		36			2.7	1.9	0.3	0.3
CARWYO-WK-H69-15F	*Carlson et al.* [1999]	47.07	−109.43	4.2	2.98–3.3	4–7.2	Intraplate craton	Peridotite	0.203	0.519	0.346	0.079	0.068	0.015		0.019	0.059	0.01	0.07	0.012	45			0.16		1.08		17			0.5	0.57	0.03	0.006
CARWYO-WK-H81-21	*Carlson et al.* [1999]	47.07	−109.43	5.4	2.98–3.3	4–7.2	Intraplate craton	Peridotite	21–1	2.2	4.3	1.6	0.5	0.09		0.2	0.06					57					12	36				6	0.85
CARWYO-WK-T3-4	*Carlson et al.* [1999]	47.07	−109.43	4.8	2.98–3.3	4–7.2	Intraplate Craton	Peridotite	21–1	2.2	4.3	1.6	0.5	0.09		0.2	0.06					57					12	36				6	0.85
CARWYO-WK-WP28-3-1	*Carlson et al.* [1999]	47.07	−109.43	3.8	2.98–3.3	4–7.2	Intraplate craton	Peridotite	21–3	9.5	15	5.4	0.9	0.21		0.4	0.1	0.1		0.2		137					25	58				12	2.95
KOPCANA-JK-21-1	*Kopylova et al.* [1999]	65.9986	−111.4792	3.1	4–4.8	6.6–7.2	Intraplate craton	Peridotite	23–5	2.9	5.1	1.9	0.6	0.2		0.5	0.18	0.3		0.4	0.09	102					9	45			3	11	1.4
KOPCANA-JK-21-3	*Kopylova and Russell* [2000]	65.9986	−111.4792	4.9	4–4.8	6.6–7.2	Intraplate craton	Peridotite	9–10	4.6	7.1	3.4	1	0.23		0.7	0.13	0.3		0.2	0.08	167					16	96			3	14	0.8
KOPCANA-JK-23-5	*Kopylova and Russell* [2000]	65.9986	−111.4792	5.9	4–4.8	6.6–7.2	Intraplate craton	Peridotite	9–12	2.95	4.6	1.45	0.45	0.095		0.2	0.036			0.1		90					10.5	48				5.5	0.8
KOPCANA-JK-9-12	*Kopylova et al.* [1999]	65.9986	−111.4792	2.9	4–4.8	6.6–7.2	Intraplate craton	Peridotite	3.82	12.8	11.6	3.62	1.37	0.62	3.91	0.86	2.05	0.29	1.88	0.26	25	13.2	2.07	1.61	45	2.4		82.2	0.21	401	20.8	53	0.18	0.08
PETDB-2220-UV001/04	*Agashev et al.* [2013]	66.4333	112.3167	6.0	2–5.3	6.5	Intraplate craton	Peridotite	55.3	104	42.2	7.65	2.44	0.93	5.16	0.97	2.56	0.37	2.42	0.37	616	118	3.83	49.1	54	56.5		1387	3.52	159	27	174	4.01	1.02
PETDB-2220-UV003/01	*Agashev et al.* [2013]	66.4333	112.3167	6.2	2–5.2	6.5	Intraplate craton	Peridotite	2.61	7.84	8.76	2.72	0.74	0.39	2.41	0.57	1.6	0.24	1.59	0.25	99	248	1.13	0.84	65	10.5		47.2	0.08	398	15.5	26	0.19	
PETDB-2220-UV003/02	*Agashev et al.* [2013]	66.4333	112.3167	6.5	2–5.1	6.5	Intraplate craton	Peridotite	3.21	10.6	10.8	3.37	0.98	0.53	3.03	0.58	1.6	0.22	1.37	0.2	26	1226	1.18	0.65	290	7.6		60.7	0.06	356	16	28	0.27	0.07
PETDB-2220-UV003/05	*Agashev et al.* [2013]	66.4333	112.3167	6.9	2–5.0	6.5	Intraplate craton	Peridotite	5	13.1	6.95	1.28	0.36		0.78	0.13	0.21		0.21	0.03	88	2100			1610		10	125		51	3.7	46		
PETDB-2220-UV018/04	*Agashev et al.* [2013]	66.4333	112.3167	6.2	2–5.1	6.5	Intraplate craton	Peridotite	1.7	3.9	2.4	0.33	0.15		0.39	0.07	0.18		0.17	0.02	36	2010			2030		10	43		44	1.9	18		
PETDB-2220-UV024/05	*Agashev et al.* [2013]	66.4333	112.3167	6.90	2–5.2	6.5	Intraplate craton	Peridotite	0.35	0.9	0.55	0.13	0.06		0.19	0.04	0.12		0.12	0.02	11	2700			2014		9	8		38	1.1	6		
PETDB-2220-UV027/01	*Agashev et al.* [2013]	66.4333	112.3167	6.8	2–5.3	6.5	Intraplate craton	Peridotite	0.26	0.6	0.45	0.12	0.04		0.2	0.04	0.14		0.15	0.02	13	2210			2443		8	9		38	1.1	3.5		
PETDB-2220-UV030/04	*Agashev et al.* [2013]	66.4333	112.3167	6.6	2–5.4	6.5	Intraplate craton	Peridotite	0.25	0.6	0.46	0.15	0.06		0.24	0.05	0.15		0.15	0.03	12	2240			2420		9	9		45	1.2	3.7		
PETDB-2220-UV032/04	*Agashev et al.* [2013]	66.4333	112.3167	6	2–5.5	6.5	Intraplate craton	Peridotite	1.27	2.51	1.61	0.54	0.24	0.3	2.39	0.69	2.14	0.33	2.18	0.33	6.2	650	0.52	1.69	580	1.05	68.5	143	0.1	367	19.4	24.8	0.12	0.06
PETDB-2220-UV033/04	*Agashev et al.* [2013]	66.4333	112.3167	6.5	2–5.6	6.5	Intraplate craton	Peridotite	2.33	3.7	2.51	1.07	0.45	0.39	2.82	0.72	2.05	0.32	2.02	0.3	14.6	811	0.77	1.19	568	2.27	53.9	380	0.06	53.9	19.6	35.5	0.19	0.1
PETDB-2220-UV038/02	*Agashev et al.* [2013]	66.4333	112.3167	5.9	2–5.6	6.5	Intraplate craton	Peridotite	1.71	2.97	1.44	0.33	0.16	0.07	0.49	0.11	0.29	0.04	0.29	0.05	13.3	2059	0.23	2.38	551	5.26	47.8	156	0.14	96	2.56	9.2	0.16	0.09
PETDB-2220-UV097/02	*Agashev et al.* [2013]	66.4333	112.3167	6	2–5.6	6.5	Intraplate craton	Peridotite	1.64	3.43	2.22	0.75	0.32	0.31	2.33	0.58	1.75	0.27	1.98	0.33	76.1	929	0.47	1.6	372	5.37	52.8	69	0.09	291	14	13.4	0.2	0.09
PETDB-2220-UV205/02	*Agashev et al.* [2013]	66.4333	112.3167	6.4	2–5.6	6.5	Intraplate craton	Peridotite	0.97	2.35	1.94	0.63	0.3	0.2	1.42	0.33	0.96	0.15	1.02	0.17	7.8	2187	0.35	0.9	822	0.93	41.6	68	0.05	185	7.87	11.8	0.11	0.03
PETDB-2220-UV208/02	*Agashev et al.* [2013]	66.4333	112.3167	6	2–5.6	6.5	Intraplate craton	Peridotite	2.14	4.32	2.41	0.63	0.26	0.18	1.34	0.31	0.95	0.15	1.09	0.18	30.2	4598	0.53	2.51	599	2.4	57.6	92	0.15	145	7.61	19.8	0.23	0.1
PETDB-2220-UV213/02	*Agashev et al.* [2013]	66.4333	112.3167	6.1	2–5.6	6.5	Intraplate craton	Peridotite	1.57	2.63	1.57	0.41	0.21	0.1	0.63	0.14	0.38	0.05	0.37	0.06	23.6	2856	0.24	2.11	726	1.72	31.6	100	0.15	93	3.22	8.6	0.14	0.06
PETDB-2220-UV252/02	*Agashev et al.* [2013]	66.4333	112.3167	6.4	2–5.6	6.5	Intraplate craton	Peridotite	1.27	2.93	2.58	0.95	0.4	0.37	2.71	0.67	1.96	0.31	2.19	0.35	9.4	1042	0.57	1.04	506	1.57	60.9	210	0.05	383	15.6	16.6	0.1	0.07
PETDB-2220-UV257/02	*Agashev et al.* [2013]	66.4333	112.3167	6.5	2–5.6	6.5	Intraplate craton	Peridotite	1.48	3.04	2.1	0.67	0.29	0.19	1.18	0.24	0.59	0.08	0.5	0.08	10.6	1246	0.32	1.5	724	1.8	41.4	207	0.08	229	5.46	11.3	0.14	0.08
PETDB-2220-UV268/02	*Agashev et al.* [2013]	66.4333	112.3167	5.6	2–5.6	6.6–7.2	Intraplate craton	Peridotite	1.58	2.6	1.19	0.27	0.09	0.04	0.25	0.05	0.15	0.02	0.16	0.03	12.77		0.19	2.23		6.39		25.93	0.11		1.6	9.12	0.13	0.09
PETDB-2220-UV285/02	*Agashev et al.* [2013]	66.4333	112.3167	5.7	2–5.6	6.5	Intraplate craton	Peridotite	1.06	2.02	0.96	0.2	0.07	0.04	0.25	0.05	0.13	0.02	0.12	0.02	10.27			1.68		3.94		13.66	0.09		1.41		0.11	0.03
PETDB-2220-UV285/02	*Carlson and Moore* [2004]	−28.82	27.42	3.05	4.8–5	6.5–8	Intraplate craton	Peridotite	0.97	2.16	1.18	0.26	0.1	0.07	0.49	0.11	0.31	0.05	0.32	0.05	13.45		0.18	1.72		4.18		19.08	0.13		3.08	7.62	0.09	0.02
RWCMONA-BD2234	*Carlson and Moore* [2004]	−28.82	27.42	2.64	4.8–5	6.5–8	Intraplate craton	Peridotite	1.53	3.22	1.86	0.38	0.12	0.05	0.31	0.06	0.16	0.02	0.16	0.02	19.26		0.27	2.43		7.35		28.2	0.15		1.8	12	0.14	0.05
RWCMONA-ROM-189	*Carlson and Moore* [2004]	−28.82	27.42	3.65	4.8–5	6.5–8	Intraplate craton	Peridotite	0.51	1.03	0.49	0.09	0.03	0.01	0.08	0.01	0.04	0.01	0.04	0.01	7.46		0.08	1.05		4.95		9.27	0.07		0.45	2.7	0.07	0.02
RWCMONA-ROM194A	*Carlson and Moore* [2004]	−28.82	27.42	3.76	4.8–5	6.5–8	Intraplate craton	Peridotite	1.74	3.3	1.55	0.33	0.12	0.07	0.45	0.09	0.24	0.03	0.22	0.03	28.93			2.68		12.2		28.48	0.16		2.51		0.2	0.06
RWCMONA-ROM-68	*Carlson and Moore* [2004]	−28.82	27.42	3.83	4.8–5	6.5–8	Intraplate craton	Peridotite	1.13	2.51	1.48	0.35	0.12	0.07	0.44	0.09	0.25	0.04	0.25	0.04	19.2		0.28	1.73		9.52		22.78	0.12		2.47	11.7	0.11	0.03
RWCMONA-ROM-69	*Carlson and Moore* [2004]	−28.82	27.42	3.33	4.8–5	6.5–8	Intraplate craton	Peridotite	0.55	1.21	0.72	0.17	0.06	0.03	0.17	0.03	0.1	0.01	0.11	0.02	10.52		0.14	1.16		5.31		12.54	0.09		0.99	6.29	0.06	0.02
SCHMCAN-SOM-NK1-23	*Schmidberger and Francis* [2001]	73.5	−91	2.07	4–4.8	6.6–7.2	Intraplate craton	Peridotite	1.26	2.22	0.87	0.14	0.04	0.02	0.12	0.02	0.06	0.01	0.06	0.01	9.14			1.8		4.18		12.03	0.09		0.67		0.14	0.05
SCHMCAN-SOM-NK1-3	*Schmidberger and Francis* [2001]	73.5	−91	3.93	4–4.8	6.6–7.2	Intraplate craton	Peridotite	0.58	1.13	0.55	0.12	0.04	0.02	0.15	0.03	0.08	0.01	0.07	0.01	8.12		0.12	1.12		5.64		11.43	0.06		0.83	5.3	0.07	0.02
SCHMCAN-SOM-NK1-4	*Schmidberger and Francis* [2001]	73.5	−91	3.11	4–4.8	6.6–7.2	Intraplate craton	Peridotite	0.79	1.4	0.64	0.12	0.04	0.01	0.08	0.01	0.04	0.01	0.05	0.01	7.47			1.27		7.7		16.05	0.07		0.46		0.12	0.08
SCHMCAN-SOM-NK1-5	*Schmidberger and Francis* [2001]	73.5	−91	5.45	4–4.8	6.6–7.2	Intraplate craton	Peridotite	1.05	2.19	1.19	0.27	0.09	0.05	0.31	0.06	0.17	0.02	0.17	0.03	13.07		0.15	1.25		3.66		23.06	0.07		1.85	6.1	0.17	0.04
SCHMCAN-SOM-NK1-6	*Schmidberger and Francis* [2001]	73.5	−91	4.88	4–4.8	6.6-7.2	Intraplate craton	Peridotite	1.01	1.81	0.78	0.15	0.05	0.01	0.06	0.01	0.03	0	0.03	0.01	12.84			2.05		4.29		10.66	0.12		0.33		0.1	0.03
SCHMCAN-SOM-NK1-7	*Schmidberger and Francis* [2001]	73.5	−91	5.51	4–4.8	6.6–7.2	Intraplate craton	Peridotite	0.82	1.5	0.73	0.19	0.07	0.04	0.27	0.05	0.12	0.02	0.09	0.01	9.03		0.14	1.51		3.56		8.47	0.09		1.41	6.67	0.1	0.03
SCHMCAN-SOM-NK2-1	*Schmidberger and Francis* [2001]	73.5	−91	5.15	4–4.8	6.6–7.2	Intraplate craton	Peridotite	0.47	0.81	0.4	0.1	0.03	0.02	0.09	0.02	0.04	0.01	0.04	0.01	6.45		0.06	0.88		2.15		8.16	0.07		0.53	3.31	0.06	0.02
SCHMCAN-SOM-NK2-10	*Schmidberger and Francis* [2001]	73.5	−91	3.45	4–4.8	6.6–7.2	Intraplate craton	Peridotite	0.82	1.63	0.86	0.21	0.07	0.04	0.21	0.04	0.1	0.01	0.1	0.02	20.3		0.2	1.49		5.7		16.46	0.09		1.11	9.39	0.09	0.03
SCHMCAN-SOM-NK2-2	*Schmidberger and Francis* [2001]	73.5	−91	5.47	4–4.8	6.6–7.2	Intraplate craton	Peridotite	0.64	1.31	0.62	0.15	0.06	0.04	0.29	0.06	0.19	0.03	0.2	0.04	14.36		0.07	0.98		4.79		48.18	0.06		1.95	3.66	0.06	0.02
SCHMCAN-SOM-NK2-3	*Schmidberger and Francis* [2001]	73.5	−91	2.34	4–4.8	6.6–7.2	Intraplate craton	Peridotite	1.39	2.8	1.51	0.29	0.09	0.05	0.32	0.07	0.19	0.03	0.21	0.04	27.92		0.26	2.44		6.79		29.62	0.25		2.15	12.6	0.18	0.05

Table 3. (continued)

Sample Name	Source	Latitude	Longitude	Pressure (Gpa)	MLD (GPa)	LAB (Gpa)	Geologic Setting	Xenolith Type	La	Ce	Nd	Sm	Eu	Tb	Dy	Ho	Er	Tm	Yb	Lu	Ba	Cr	Hf	Nb	Ni	Rb	Sc	Sr	Ta	V	Y	Zr	Th	U
SCHMCAN-SOM-NK3-1	*Schmidberger and Francis* [2001]	73.5	−91	1.7	4–4.8	6.6–7.2	Intraplate craton	Peridotite	0.61	1.01	0.47	0.11	0.04	0.02	0.13	0.03	0.07	0.01	0.08	0.01	14.94		0.06	1.32		3.82		15.08	0.08		0.81	2.55	0.06	0.02
SCHMCAN-SOM-NK2-7	*Schmidberger and Francis* [2001]	73.5	−91	1.7	4–4.8	6.6–7.2	Intraplate craton	Peridotite													113	2564		7.2	2161	7.7		38		29	2.2	12		
SCHMCAN-SOM-NK3-15	*Schmidberger and Francis* [2001]	73.5	−91	5.11	4–4.8	6.6–7.2	Intraplate craton	Peridotite													69	2588		4.8	2022	7.8		57		33	2.2	13		
SCHMCAN-SOM-NK3-24	*Schmidberger and Francis* [2001]	73.5	−91	1.75	4–4.8	6.6–7.2	Intraplate craton	Peridotite													184	4686		4.8	1282	17.7		30		71	1.7	15		
SCHMCAN-SOM-NK3-20	*Schmidberger and Francis* [2001]	73.5	−91	3.1	4–4.8	6.6–7.2	Intraplate craton	Peridotite													76	2799		5.8	1954	12.1		43		36	5.2	26		
KOPCANA-JK-9-10	*Kopylova and Russell* [2000]	65.9986	−111	5.7	4–4.8	6.6–7.2	Intraplate craton	Pyroxenite													37	1839		3.1	2302	2.9		25		24	2.2	15		
PETDB-2018-BSK-12	*Yu et al.* [2010]	43.3	125	1.7	2	3–3.5	Intraplate craton	Pyroxenite													70	2041		7.7	2153	10.3		45		28	1.7	15		
PETDB-2018-BSK-13	*Yu et al.* [2010]	43.3	125	1.6	2	3–3.5	Intraplate craton	Pyroxenite	8.38	12.26	3.68	0.562	0.17	0.094	0.517	0.112	0.319	0.051	0.331	0.055	105		0.206	8.42		4.72		86.5	0.11		3.45	8.08	0.939	0.129
PETDB-2018-YQSX-12	*Yu et al.* [2010]	43.3	125	1.0	2	3–3.5	Intraplate craton	Pyroxenite	1.88	3.56	1.73	0.368	0.119	0.058	0.306	0.06	0.156	0.024	0.154	0.026	22.2		0.104	2.22		1.72		56.3	0.09		1.84	6.79	0.199	0.098
PETDB-2018-YQSX-13	*Yu et al.* [2010]	43.3	125	1.1	2	3–3.5	Intraplate craton	Pyroxenite	1.99	3.46	1.45	0.226	0.066	0.032	0.208	0.048	0.132	0.02	0.142	0.025	45.6		0.079	1.67		3.03		43.3	0.06	44.7	1.3	3.53	0.209	0.059
PETDB-2018-YQSX-18	*Yu et al.* [2010]	43.3	125	1.6	2	3–3.5	Intraplate craton	Pyroxenite	1.44	2.57	1.15	0.264	0.093	0.058	0.337	0.062	0.147	0.021	0.141	0.025	27.9		0.207	1.76		4.29		46.5	0.11		1.8	8.81	0.177	0.078
PETDB-2018-YQSX-19	*Yu et al.* [2010]	43.3	125	1.1	2	3–3.5	Intraplate craton	Pyroxenite	0.69	1.82	0.97	0.22	0.073	0.05	0.28	0.06	0.16	0.025	0.16	0.026	18		0	1.2		0.8		17.1	0.06	25	1.6	7	0.24	0
PETDB-2018-YQSX-2	*Yu et al.* [2010]	43.3	125	1.3	2	3–3.5	Intraplate craton	Pyroxenite	0.5	0.875	0.448	0.143	0.047	0.023	0.134	0.031	0.094	0.018	0.124	0.021	10.5		0.077	0.6		1.03		15.2	0.04		0.92	3.31	0.061	0.012
PETDB-2018-YQSX-4	*Yu et al.* [2010]	43.3	125	1.3	2	3–3.5	Intraplate craton	Pyroxenite	0.51	1.42	0.63	0.14	0.046	0.03	0.15	0.03	0.07	0.008	0.05	0.008	23		0.1	1.3		10		31.3	0.1	32	0.7	4.3	0.18	0
PETDB-2018-YQSX-7	*Yu et al.* [2010]	43.3	125	1.2	2	3–3.5	Intraplate craton	Pyroxenite	5.21	8.58	3.48	0.559	0.158	0.072	0.338	0.063	0.17	0.024	0.152	0.025	82		0.115	3.51		2.99		92.6	0.11		1.96	6.85	0.495	0.187
SCHMCAN-SOM-NK3-14	*Schmidberger and Francis* [2001]	73.5	−91	3.6	4–4.8	6.6–7.2	Intraplate craton	Pyroxenite	5.35	7.94	2.58	0.402	0.128	0.057	0.341	0.087	0.255	0.036	0.302	0.04	93.9		0.182	3.71		7.52		77.7	0.09	54.7	2.52	6.56	0.598	0.193
SCHMCAN-SOM-NK3-17	*Schmidberger and Francis* [2001]	73.5	−91	1.8	4–4.8	6.6–7.2	Intraplate craton	Pyroxenite	19.3	27.3	5.13	0.91	0.28	0.21	1.28	0.3	0.9	0.147	0.94	0.139	148		0.3	6.5		4.1		284	0.05	156	8.3	9.4	1.45	0.8
FALHUNG-PAN-GC03-06	*Falus et al.* [2007]	47.5	18.5	0.9	N/A	3.98–4.9	Intraplate off-craton	Peridotite	2.59	5.89	3.4	0.768	0.241	0.173	1.08	0.244	0.705	0.102	0.659	0.099	50		0.345	1.46		5.06		90.3	0.09		7.14	10.2	0.226	0.05
JANSLOV-POH-119-5	*Janak et al.* [2006]	46.4	15.5	4.0	N/A		Intraplate off-craton	Peridotite	19.3	27.3	5.13	0.91	0.28	0.21	1.28	0.3	0.9	0.147	0.94	0.139	148		0.3	6.5		4.1		284	0.05	156	8.3	9.4	1.45	0.8
JANSLOV-POH-VI01/04	*Janak et al.* [2006]	46.4	15.5	3.4	N/A		Intraplate off-craton	Peridotite	2.09	3.4	1.19	0.215	0.093	0.025	0.125	0.021	0.051	0.007	0.05	0.015	23.3		0.131	1.5		3.66		344	0.09	34	0.48	5.56	0.221	0.779
PETDB-1908-101892	*Orejana et al.* [2006]	40.5	−4.1	1.1	N/A	1.6–2	Intraplate off-craton	Pyroxenite	8.68	16.65	7.86	1.62	0.654	0.335	2.52	0.541	1.48	0.264	1.53	0.298	451		0.685	16.1		30.2		162	1.09	117	16.1	39.5	0.86	0.897
PETDB-1908-101892	*Orejana et al.* [2006]	40.5	−4.1	1.1	N/A	1.6–2	Intraplate off-craton	Pyroxenite	2.2	4.17	2.13	0.68	0.223	0.19	1.18	0.27	0.77	0.127	0.76	0.109	71		0.2	1.4		3.6		38.8	0.03	221	7.1	4.8	0.35	0.15
PETDB-1908-102131	*Orejana et al.* [2006]	40.5	−4.1	1.1	N/A	1.6–2	Intraplate off-craton	Pyroxenite	2.05	3.48	1.16	0.17	0.052	0.026	0.152	0.037	0.119	0.02	0.14	0.026	51.2		0.048	2.11		3.66		128	0.08		1.14	2.03	0.238	0.416
PETDB-1908-104395	*Orejana et al.* [2006]	40.5	−4.1	0.9	N/A	1.6–2	Intraplate off-craton	Pyroxenite	3.19	4.08	1.52	0.299	0.112	0.059	0.423	0.099	0.33	0.043	0.342	0.05	82.5		0.182	2.46		7.33		55.9	0.04	80	3.04	5.57	0.265	0.125
MLX																																		
SCHMCAN-SOM-NK1-12	*Schmidberger and Francis* [2001]	73.5	−91	4.06	4–4.8	6.6–7.2	Intraplate craton	Peridotite	2.62	5.22	2.21	0.4	0.11	0.04	0.21	0.04	0.1	0.014	0.07	0.013	126		0.2	3.1	-	3.2	-	56.5	0.17	18	1	8.9	0.37	0.06
SCHMCAN-SOM-NK1-15	*Schmidberger and Francis* [2001]	73.5	−91	4.16	4–4.8	6.6–7.2	Intraplate craton	Peridotite	2.31	4.99	2.03	0.258	0.076	0.035	0.173	0.043	0.117	0.022	0.128	0.026	27.4		0.064	2.03	-	1.43	-	43.7	0.07	36.3	1.23	3.02	0.2	0.055
SCHMCAN-SOM-NK1-14	*Schmidberger and Francis* [2001]	73.5	−91	4.25	4–4.8	6.6–7.2	Intraplate craton	Peridotite	5.01	9.22	3.85	0.59	0.15	0.053	0.186	0.028	0.076	0.008	0.055	0.008	89.6		0.214	6.36	-	7.25	-	66.7	0.31		0.83	9.91	0.644	0.093
SCHMCAN-SOM-NK1-9	*Schmidberger and Francis* [2001]	73.5	−91	4.35	4–4.8	6.6–7.2	Intraplate craton	Peridotite	0.972	1.97	0.922	0.249	0.086	0.035	0.234	0.046	0.106	0.016	0.104	0.017	14.8		0.145	1.2	-	1.53	-	17.8	0.08	35.5	1.18	6.31	0.131	0.027
SCHMCAN-SOM-NK1-2	*Schmidberger and Francis* [2001]	73.5	−91	4.47	4–4.8	6.6–7.2	Intraplate craton	Peridotite	1.92	4.16	1.87	0.285	0.079	0.029	0.169	0.035	0.098	0.014	0.099	0.016	18.9		0.045	1.7	-	1.15	-	33.8	0.07	30.5	0.88	2.86	0.165	0.031
SCHMCAN-SOM-NK3-4	*Schmidberger and Francis* [2001]	73.5	−91	4.49	4–4.8	6.6–7.2	Intraplate craton	Peridotite	3.26	5.37	2.21	0.421	0.154	0.08	0.489	0.113	0.335	0.055	0.366	0.06	50.6		0.237	2.45	-	23.2	-	245	0.15		3.5	9.76	0.217	0.502
SCHMCAN-SOM-NK1-18	*Schmidberger and Francis* [2001]	73.5	−91	4.52	4–4.8	6.6–7.2	Intraplate craton	Peridotite	0.872	1.5	0.608	0.12	0.039	0.015	0.059	0.008	0.022	0.003	0.021	0.004	13.1		0.051	1.15	-	1.85	-	41.7	0.06		0.31	2.52	0.095	0.067
SCHMCAN-SOM-NK3-25	*Schmidberger and Francis* [2001]	73.5	−91	4.55	4–4.8	6.6–7.2	Intraplate craton	Peridotite	3.3	4.74	1.76	0.327	0.104	0.063	0.507	0.113	0.328	0.051	0.319	0.063	83.9		0.265	4.22	-	28.7	-	37.5	0.24	68.3	3.13	11.3	0.267	0.347
SCHMCAN-SOM-NK1-1	*Schmidberger and Francis* [2001]	73.5	−91	4.9	4–4.8	6.6–7.2	Intraplate craton	Peridotite	1.36	2.81	1.15	0.21	0.072	0.04	0.22	0.04	0.1	0.013	0.08	0.013	31		0.1	1.7	2.59	1.1	-	25.7	0.08	23	1.1	6.5	0.34	0.09
PETDB-2410-UV-101/03	*Doucet et al.* [2012]	66.4386	112.3167	2.5	2–5.6	6.5	Intraplate craton	Harzburgite	0.447	0.732	0.286	0.049	0.015	0.005	0.024	0.004	0.016	0.003	0.035	0.008	13.7		0.011	1.07	-	5.67	-	16.1	0.029		0.13	0.87	0.088	0.016
PETDB-2410-UV-105/03	*Doucet et al.* [2012]	66.4386	112.3167	2.5	2–5.6	6.5	Intraplate craton	Harzburgite	0.806	1.48	0.58	0.077	0.022	0.006	0.033	0.005	0.014	0.002	0.016	0.004	17.2		0.024	2.38	-	3.07	-	10.3	0.082		0.15	1.52	0.178	0.026
PETDB-2410-UV-107/03	*Doucet et al.* [2012]	66.4386	112.3167	2.5	2–5.6	6.5	Intraplate craton	Harzburgite	0.674	1.09	0.429	0.063	0.019	0.006	0.032	0.005	0.015	0.002	0.012	0.003	14.8		0.024	2.03	-	4.15	-	9.02	0.095		0.26	1.48	0.105	0.02
PETDB-2410-UV-402/09	*Doucet et al.* [2012]	66.4386	112.3167	2.5	2–5.6	6.5	Intraplate craton	Harzburgite	3.78	5.24	1.73	0.247	0.078	0.025	0.126	0.021	0.048	0.005	0.03	0.004	30.6		0.045	4.08	-	8.76	-	56.6	0.195		0.53	2.77	0.444	0.168
PETDB-2410-UV-454/09	*Doucet et al.* [2012]	66.4386	112.3167	2.5	2–5.6	6.5	Intraplate craton	Harzburgite	1.2	1.97	0.604	0.067	0.018	0.004	0.027	0.006	0.021	0.004	0.028	0.005	11.2		0.009	1.42	-	1.84	-	15.2	0.027		0.16	0.68	0.165	0.044
PETDB-2410-UV-487/09	*Doucet et al.* [2012]	66.4386	112.3167	2.5	2–5.6	6.5	Intraplate craton	Harzburgite	4.83	7.46	2.398	0.304	0.093	0.025	0.123	0.018	0.045	0.005	0.028	0.004	22.3		0.068	10.3	-	13.2	-	47.6	0.696		0.45	3.88	1.39	0.18
PETDB-2410-UV-504/09	*Doucet et al.* [2012]	66.4386	112.3167	2.5	2–5.6	6.5	Intraplate craton	Harzburgite	0.883	1.51	0.594	0.083	0.034	0.007	0.034	0.005	0.013	0.002	0.013	0.002	17.7		0.035	1.87	-	6.96	-	22.2	0.101		0.18	2.41	0.153	0.018
PETDB-2410-UV-585/09(1)	*Doucet et al.* [2012]	66.4386	112.3167	2.5	2–5.6	6.5	Intraplate craton	Harzburgite	1.28	2.21	0.984	0.172	0.049	0.012	0.058	0.009	0.023	0.003	0.02	0.005	20.6		0.017	1.61	-	8.63	-	16.5	0.029		0.26	1.44	0.192	0.054
PETDB-2410-UV-585/09(2)	*Doucet et al.* [2012]	66.4386	112.3167	2.5	2–5.6	6.5	Intraplate craton	Harzburgite	1.4	2.36	1.04	0.186	0.054	0.013	0.057	0.008	0.022	0.003	0.021	0.004	19.6		0.016	1.54	-	9.06	-	19.4	0.027		0.26	1.45	0.203	0.062
PETDB-2410-UV-590/09	*Doucet et al.* [2012]	66.4386	112.3167	2.5	2–5.6	6.5	Intraplate craton	Harzburgite	1.5	2.61	0.867	0.101	0.029	0.006	0.027	0.004	0.01	0.001	0.006	0.001	15.9		0.021	2.4	-	0.82	-	20.4	0.089		0.1	1.45	0.187	0.042
PETDB-2410-UV-600/09	*Doucet et al.* [2012]	66.4386	112.3167	2.5	2–5.6	6.5	Intraplate craton	Harzburgite	0.719	1.38	0.668	0.105	0.044	0.01	0.049	0.008	0.022	0.003	0.027	0.006	35.3		0.1	2.01	-	8.2	-	15.3	0.085		0.26	5.71	0.107	0.021
PETDB-2410-UV-90/03	*Doucet et al.* [2012]	66.4386	112.3167	2.5	2–5.6	6.5	Intraplate craton	Harzburgite	3.53	6.66	2.39	0.291	0.079	0.018	0.081	0.011	0.031	0.004	0.022	0.004	19.7		0.041	8.86	-	16.2	-	31	0.254		0.34	4.3	0.73	0.087
PETDB-2410-UV-KC-137/08	*Doucet et al.* [2012]	66.4386	112.3167	2.5	2–5.6	6.5	Intraplate craton	Harzburgite	1.72	2.77	0.902	0.117	0.034	0.01	0.047	0.007	0.018	0.002	0.011	0.002	9.36		0.025	4.18	-	1.66	-	7.24	0.436		0.2	1.5	0.189	0.068
PETDB-2410-UV-KC-150(2)/08	*Doucet et al.* [2012]	66.4386	112.3167	2.5	2–5.6	6.5	Intraplate craton	Harzburgite	1.23	2.05	0.703	0.091	0.027	0.007	0.036	0.006	0.015	0.002	0.012	0.002	11.5		0.031	3.06	-	4.76	-	9.92	0.116		0.17	2.08	0.161	0.037

references therein]. The boundary is called the MLD in some studies and the LAB in others, with the distinction between the two features ambiguous. Velocity decreases and transition thicknesses are most robust when obtained through inversion of synthetic receiver functions [e.g., *Rychert et al*., 2007]; however, for many studies, additional steps to determine detailed characteristics of the boundary are not attempted. Nevertheless, many receiver function studies identify relatively sharp velocity decreases within the continental lithosphere of ~5% at depths of 60–160 km (Table 1).

3.4. Underside Reflections

The underside reflection of shear and compressional wave energy from upper mantle seismic discontinuities produces precursory arrivals to the seismic phases SS and PP, as well as pP and sS depth phases from deep earthquakes. SS and PP precursors have been used extensively to map the lateral variations in the depth and sharpness of upper mantle discontinuity structure around the globe [e.g., *Shearer*, 1990; *Gu et al*., 1998; *Flanagan and Shearer*, 1998]. This technique has only recently been applied routinely to imaging structure in the 60–160 km depth range, although it is predominantly applied to oceanic regions [*Rychert and Shearer*, 2011; *Schmerr*, 2012]. Nonetheless, sparse observations of the MLD with SS and PP precursors in continental settings exist [*Heit et al*., 2010], though a global survey has yet to be conducted using these seismic phases. Sampling points within a single survey are often clustered at depths of ~90 km, comparable to depths measured by the other seismic techniques. Precursors reflect from significantly greater depths under regions of active tectonics. Velocity deviations are rarely reported but are around −5% Vs [*Heit et al*., 2010].

3.5. ScS Reverberations

The ScS reverberation technique utilizes transversely polarized shear wave energy that reflects and reverberates from the core, crust, and seismic impedance contrasts in the upper and lower mantle. The multiple reverberations are typically used to produce a reflectivity profile of the mantle and where above the background noise, are indicative of seismic discontinuities within the Earth [*Revenaugh and Jordan*, 1991]. The observations are typically made in corridors that stretch between a source region of earthquakes and a series of seismic stations and utilize relatively long period (>30 s low-pass filtered) data. ScS reverberation investigations are predominantly beneath the oceanic regions, but there are a few studies in continental regions [e.g., *Revenaugh and Sipkin*, 1994; *Courtier and Revenaugh*, 2006]. In addition to detecting positive velocity contrasts with depth, such as the Hales discontinuity (80–100 km) and the Lehmann discontinuity (200–250 km), some regions, such as China and the eastern United States, exhibit evidence for a sharp (10–20 km thick) velocity decrease with depth (5–12% decrease in shear velocity, assuming the reflectance is only due to velocity and not density) over a depth of 80–130 km.

3.6. Summary of Seismic Results

Taken together, the seismic observations indicate the widespread occurrence of low-velocity layers within the interior of thick continental lithosphere (Figure 3). There is a strong regional bias in any analysis owing to the abundance of seismic data beneath the continental United States from the recent Earthscope Transportable Array. To account for this regional bias in our statistics, we consider regions that are most heavily studied by averaging the observations by geographic area (Figure 4), which reveals that while MLDs are detected at many locales and at various depths (from 60 to 160 km), the majority of detections occur at ~80–100 km deep. Regions with the most consistent detection of the MLD include the central United States, South Africa, Northern Eurasia, and Australia, and coincide with the best-studied locales.

4. Xenoliths

For our analysis of the xenoliths, we found 174 of the 12,246 xenoliths in the global database PetDB (Tables 2 and 3) contained depth information as well as either whole-rock trace element concentrations or C or H bearing minerals. Of the subset matching these criteria, at least 30 xenoliths contain reported carbonate or graphite and come from depths that range between 0.9 and 2 GPa. Forty-four xenoliths are reported to bear amphibole or phlogopite and come from depths of 0.2–6.5 GPa (Table 2, Figure 5). Phlogopite is far more common in xenoliths that crystallize >2 GPa, at least partly due to the instability of amphibole at pressures greater than 3 GPa. Unfortunately, there is insufficient mineralogical data for xenoliths in the database to significantly compare specific depths in different tectonic settings. Better reporting of the global

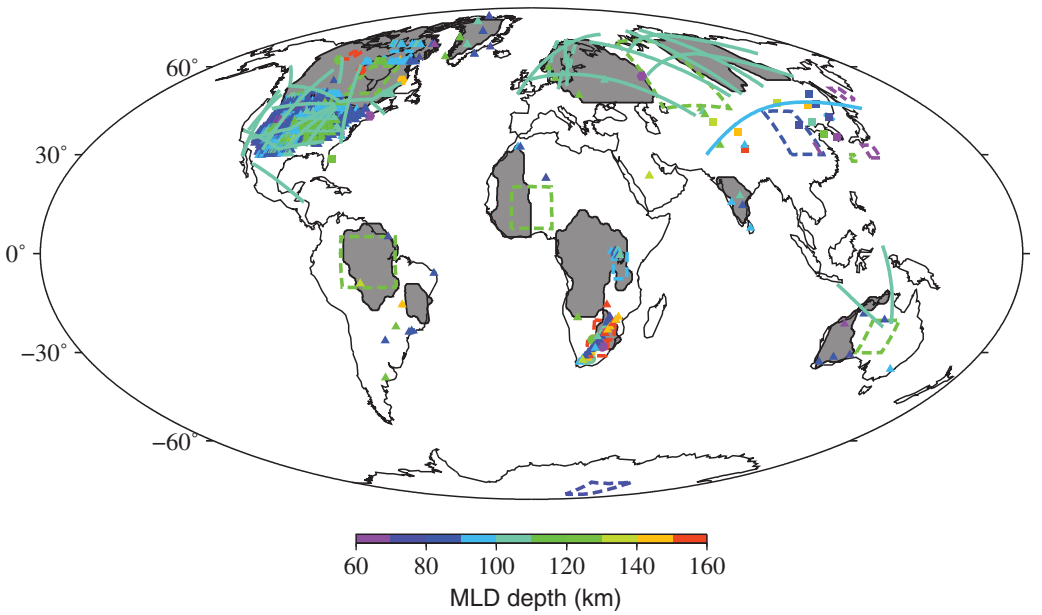

Figure 3. Geographic distribution of seismic detections of the MLD. Observations and references are cataloged in Table 1. Cratonic bodies are indicated in gray. The symbol for each observation indicates the method used and the color indicates the depth at which the MLD was identified. Boxes with broken boundaries are surface waves or regions of multiple receiver functions, individual squares are the midpoints locale of ScS reverberation corridors, triangles are individual receiver function stacks, hexagons are anisotropic studies, diamonds are SS precursors, and solid lines are active source studies.

occurrence of phlogopite, amphiboles, and carbonate minerals in xenoliths will further explain the origin of the MLD.

One hundred and five xenoliths had published analyses for trace element concentrations (Table 3). There are four xenoliths that contained both trace element concentrations (Table 3) and mineralogical data (Table 2). These samples have the same name, but may have different references as the analyses were published at different times.

We refer to xenoliths that originate from depths and locales that coincide with where the MLD is been seismically observed as midlithosphere discontinuity associated xenoliths or MLX. MLX have on average 85% lower concentrations of mildly incompatible elements such as (Zr, Hf, Y, Ho, Er, Yb, and Lu) than their non-MLX counterparts where the MLD is not seismically observed (Table 3 and Figure 6). However, there is not a significant difference in the more-incompatible elements within the population of MLXs than in non-MLXs. Additionally, there is no difference in elements typically enriched in phlogopite, such as Ba and Rb.

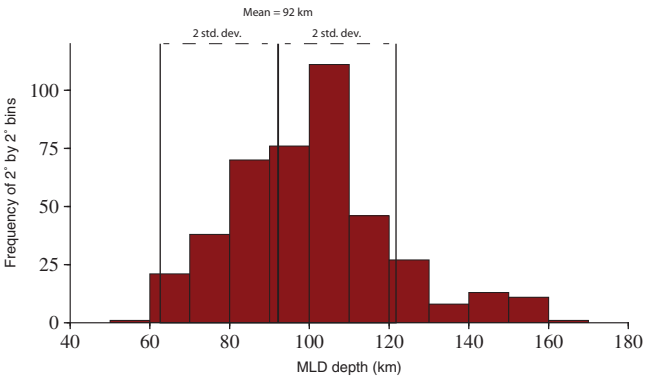

Figure 4. Spatial frequency of observed depths of the MLD. Geographic occurrences are averaged into 2° × 2° bins across the globe to avoid geographic sampling biases [e.g., *Kumar et al.*, 2012]. Histogram bins are 10 km.

The mildly incompatible elements in the MLXs, in ppm, range between 0.286 and 3.85 for Nd, 0.68 and 11.3 for Zr, 0.009 and 0.265 for Hf, 0.049 and 0.59 for Sm, 0.015 and 0.154 for Eu, 0.1 and 3.5 for Y, 0.006 and 0.366 for Yb, 0.001 and 0.063 for Lu, 0.004 and 0.113 for Ho, and 0.01 and 0.335 for Ho (Figure 7). These concentrations are systematically lower than the non-MLX concentrations of 0.346–42.2 for Nd, 0.57–174 for Zr, 0–3.83 for Hf, 0.079–7.65 for Sm, 0.03–2.44 for Eu, 0.16–27 for Y, 0.011–2.42 for Yb, 0.001–0.4 for Lu, 0.002–0.97 for Ho, 0.009–2.56 for Er (Table 3). The mildly incompatible trace

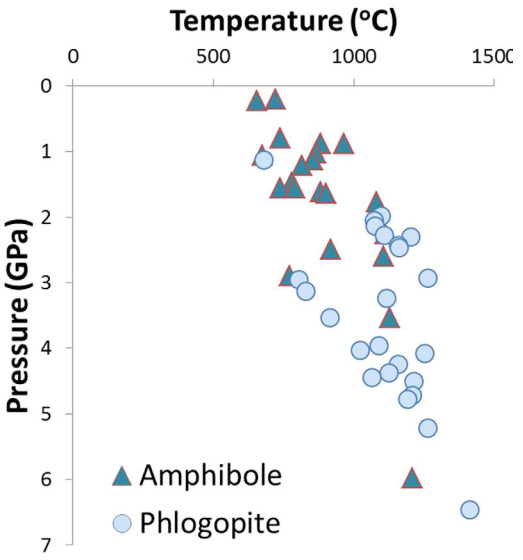

Figure 5. Pressure and temperature range of hydrous mineral-bearing xenoliths (Table 2). Dark triangles are xenoliths containing amphibole and lighter circles represent xenoliths that contain phlogopite. Error bars show the potential deviation from the expected result for the *Brey and Köhler* [1990] ol-cpx-opx-gt thermobarometer.

elements in MLXs have lower concentrations than depleted mantle. Non-MLXs typically have higher concentrations of the mildly incompatible trace elements than depleted mantle and are less likely to overlap with analyses of hydrous and carbonate minerals (Figure 7). Therefore, although the concentrations of mildly incompatible elements agree with a ponded and stalled melt at depths consistent with where the MLD is seismically observed, the more-incompatible elements (i.e., Rb and Ba), which should be present in higher quantities in phlogopite, exhibit the opposite relationship. One possible explanation for this apparent inconsistency is that previous partial melts extracted the more-incompatible elements and transported them to the surface. These final melts that became trapped were generated from an already depleted source, hence lower Rb and Ba concentrations.

5. Discussion

5.1. Seismic Characteristics of the MLD

The MLD is consistently observed across many methods including receiver functions on P and S waves, SS or PP precursors, surface waves, and active source (Table 1). The boundary is detected beneath cratons on almost every continent where there is sufficient seismic coverage (Figure 3). Reported depths at which shear velocity decreases occur are as shallow as 47 km, and models from active source studies require low velocity layering extend as deep as 300 km [*Thybo and Perchuc*, 1997]. The histogram in Figure 4 shows the discontinuity depth clusters around 80–100 km with a small secondary peak at 140–150 km; although it has been recently proposed that MLD depths may be biased by use of low-frequency receiver functions (see Supporting Information Figure S7 and S8 for more discussion). This wide range of depths of the MLD appears mostly insensitive to pressure, making a phase transition origin unlikely. The measured range of sharp seismic velocity decreases is 2–7% and prior modeling results suggest that this decrease is followed by an increase back to the regular gradient over a range of about 10 km [*Rychert et al.*, 2010]. The seismic database shows that the boundary is consistently observed within the interiors of thick, ancient cratons; however, the distinction between MLD and LAB is more tenuous along the edges of stable continental lithosphere and the two discontinuities may be coincident [e.g., *Abt et al.*, 2010; *Ford et al.*, 2010]. Given the density of coverage provided by the EarthScope Transportable Array, the region with the most observations is the North American craton, where the discontinuity is 80–115 km below the surface. This database of observations is expected to expand as new seismic deployments fill in some of the less well-covered regions.

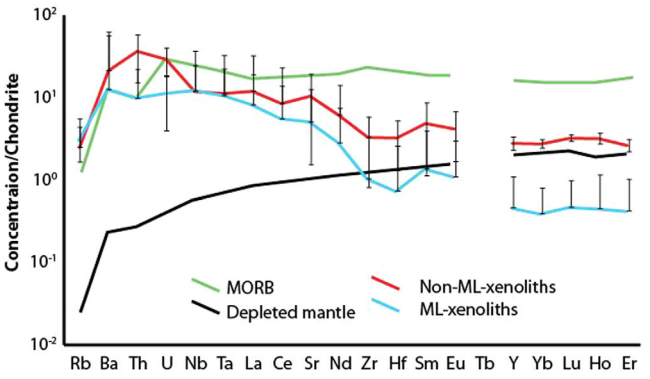

Figure 6. Trace element concentrations normalized to C-1 chondrite for xenoliths sampling the continental lithosphere [*Sun and McDonough*, 1989]. Average of 23 samples from depths and regions where the MLD has been seismically detected (MLX, blue line) and the average of 80 samples from continental regions or depths where no MLD is detected (non-MLX, red line). Details and references for individual samples used here are found in Table 3. Depleted mantle is shown as a black line [*Workman and Hart*, 2005], mid-ocean ridge basalt (MORB) is shown by a green line [*Kelemen et al.*, 2003]. Error bars on xenoliths are 1σ.

5.2. Shear Wave Velocity Modeling

The elastic parameters of hydrous minerals have been compiled for subduction zones and other tectonic

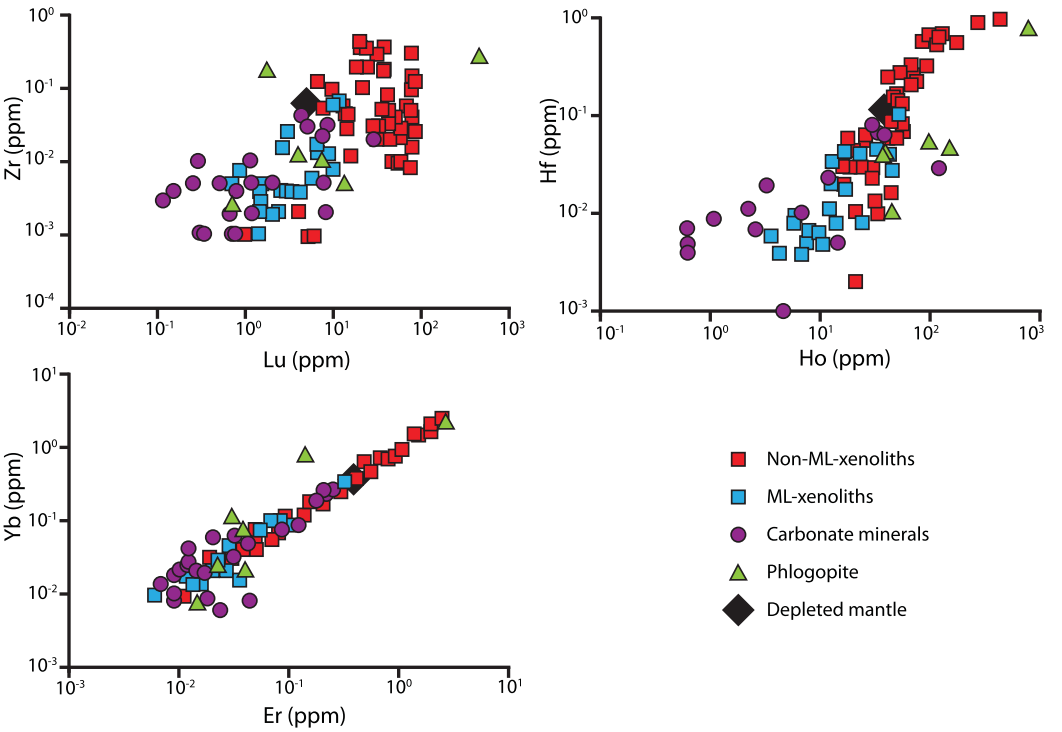

Figure 7. Selected trace element concentrations for xenoliths from depths and regions where the MLD has been identified (blue squares) and regions or depths where it has not (red squares). Xenoliths from different regions of the mantle (in the MLD or not in the MLD) can be distinguished by their concentration of low-incompatibility trace elements. The overlap between carbonate minerals (purple circles) and phlogopite (green triangles) and MLXs suggests concentrated crystallized melt might be responsible for the shear velocity decrease seen at the MLD. Depleted mantle [*Workman and Hart*, 2005] is shown as a black diamond. Error is reported in each study and is usually less than 5–10%.

settings [e.g., *Hacker et al*., 2003]. To model the relative shear velocity reduction associated with different mineral modes, we compare the contribution of individual minerals to a reference peridotite (4.75 km/s; Figure 8). Mineral velocities for a wide variety of mantle minerals were obtained from *Hacker et al*. [2003] at 1 GPa and 600°C to approximate continental lithosphere conditions. Using the seismic properties of hydrous and carbonate minerals from *Hacker et al*. [2003], we calculate the individual mineral mode necessary to achieve the magnitude of shear velocity decrease characteristic observed at the MLD (blue shading). This simple calculation assumes a background of peridotite and adds an increasing fraction of the extra mineral, obtaining seismic properties by averaging the velocity and density of peridotite with the relative fraction of an extra mineral. It does not account for phase relationships or chemical equilibria between minerals. Figure 8 shows that the observed range of decrease in shear velocity (2–7%) can be achieved by adding 5–15% of the mineral phlogopite or 10–25% of carbonate minerals at 1 GPa. A similar amount of the extra mineral can be added at higher pressure and achieve the same effect. Mineralogical data suggest the presence of phlogopite in xenoliths that equilibrated between 2 and 5 GPa (Figure 5). Therefore, based on this simple analysis, phlogopite presents an attractive candidate for the origin of the larger seismic velocity decreases (5–7%) observed at the MLD.

To produce a more quantitative assessment of properties, and to explore a wider variety of lithologies than represented in the xenolith database, we use Perple_X [*Connolly*, 2005] to model the density and seismic velocities of mantle carbonatites, eclogites, pyroxenites, Si-depleted nephelinite melts (which has been suggested as the residual product of metasomatism in the mantle), and both spinel-rich and garnet-rich peridotites (Figure 9). Perple_X uses a free-energy minimization algorithm developed by *Ita and Stixrude* [1992] to calculate stable assemblages over a range of pressures and temperatures for the system of Na_2O, MgO, MnO, TiO_2, Al_2O_3, SiO_2, K_2O, CaO, FeO, Cl_2, Fe_2O_3, H_2O, and CO_2. We used Perple_X to calculate phase diagrams for pressures from 1.5 to 8 GPa, and 500 to 1200°C for the above lithologies. Density, P-wave, and S-wave velocities are then calculated as a Hill average of the Voigt-Reuss bounds on the elastic properties for different percentages of the constituent minerals to obtain a bulk rock velocity and density.

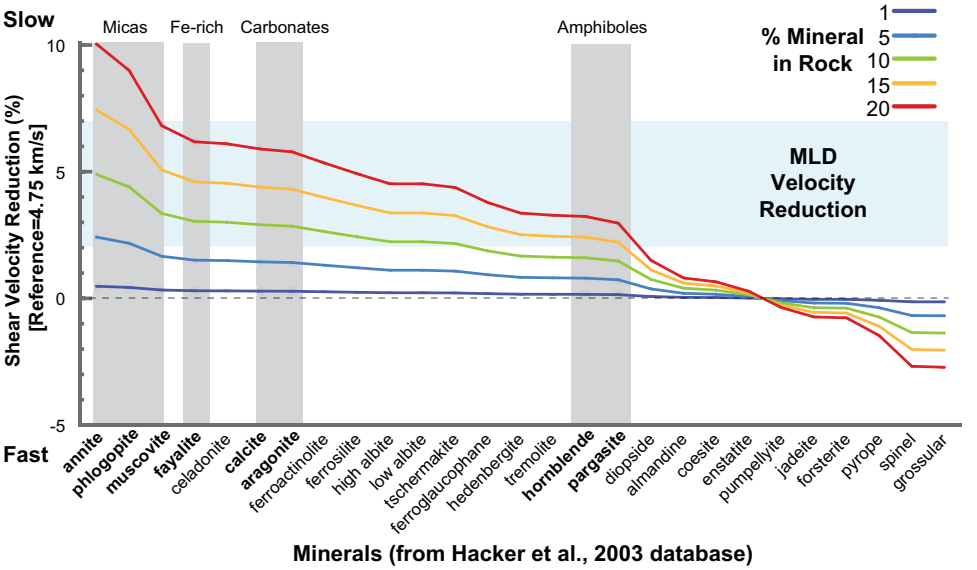

Figure 8. The shear velocity reduction resulting from a Voigt-Reuss average of peridotite and a fractional percentage of extra minerals. A reference velocity of 4.75 km/s was used for mantle peridotite at 1 GPa, all mineral properties are calculated from the database of *Hacker et al*., [2003]. Colored lines are for various percentages of the extra minerals. Minerals of particular interest include iron-rich minerals, micas, carbonates, and amphiboles (gray shading). The range of the MLD velocity reductions observed in the seismic database is shaded in blue.

Combinations of pressures and temperatures that result in melt were excluded as we are seeking the elastic parameters of solid lithologies, as suggested by the low geothermal gradient in continental cratonic environments.

At 1.5 GPa and 600°C, lithologies with 10–30% carbonatite, 40–100% cpx-pyroxenite or Si-depleted melt, or 55–100% carbonated eclogite reproduce observed shear velocity reductions at the MLD (Figure 9). Carbonatitic compositions are predicted to be 2–3% less dense than surrounding peridotites, and such a layer with a mixture of carbonatitic lithology would be buoyantly unstable over a billion year time scale. Si-depleted rocks, opx-pyroxenites, and carbonated eclogite are both denser (2–5%) than the surrounding peridotite, and would similarly introduce a buoyantly unstable layer of material into the continental lithosphere. Such features would be readily removed during episodes of continental modification or initiation of Rayleigh-Taylor instabilities [e.g., *Poudjom Djomani et al*., 2001]. Of the lithologies we investigated, only cpx-pyroxenite appears to have the necessary properties to both reproduce the observed velocity contrast and remain neutrally buoyant over the timescales of continental lithosphere evolution.

5.3. A Stalled Melt Layer?

In mantle peridotite, the fluid-saturated solidus has a distinct near-horizontal segment at ~950–1200°C and ~2 GPa [*Falloon and Green*, 1989]. Melt that is generated deeper and is in thermal equilibrium with surrounding peridotite would tend to solidify at the gently sloping part of the solidus over a broad range of geothermal gradients as the mantle lithosphere cools (Figure 10). The pressure at which aging geothermal gradients intersect the volatile-rich solidus is equivalent to a depth of ~100 km and is coincident with the majority of observed depths of the MLD. We postulate that as the lithospheric mantle cools over time, the crystallization of melt develops a permeability cap at shallower depth, concentrating melt into a melt compaction layer that will subsequently sharpen the associated seismic discontinuity [*Sparks and Parmentier*, 1991; *Revenaugh and Meyer*, 1997]. Subsequent alteration of the continental lithosphere may follow this initial, ancient formation phase. Examples of secondary alteration and formation of a deeper MLD are evidenced in parts of South America by *Heit et al*, [2007], as well as beneath South Africa where *Sodoudi et al*, [2013] image-layered structure within the lithosphere. Furthermore, *Savage and Silver* [2008] make the argument that the lithosphere beneath South Africa experienced a secondary emplacement of frozen melts.

Figure 7 indicates that xenoliths from regions where the MLD is present (MLX) are chemically distinct from xenoliths from depths or regions where no MLD has been detected (non-MLX). Mildly incompatible trace

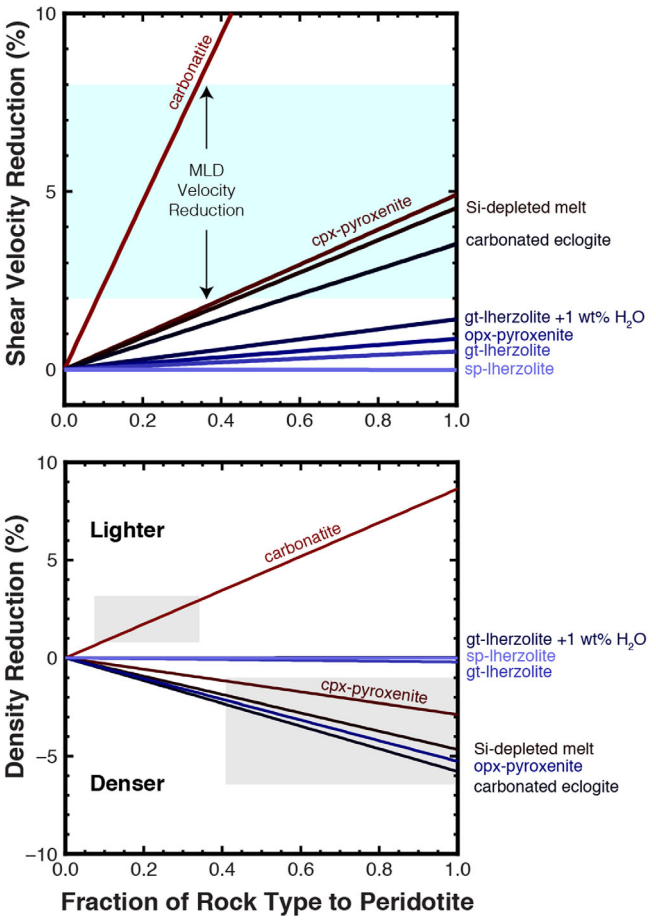

Figure 9. Perple_X models of elastic properties for candidate mantle rock mixtures. The shear velocity for each mixture of peridotite and associated modified lithology is calculated with the Hill average of a Voigt-Reuss mixture of the two lithologies (see section 5.2). The range of the shear velocity contrast observed by the seismic methods (cyan shading) fixes the fractional amounts allowed for each rock type. The fractional amount is used to determine the range of allowable densities in the plot (gray-shaded regions).

elements (Lu, Hf, Ho, Yb, Y, Er, Zr, Nd) of MLX have lower concentrations than either the depleted mantle or non-MLXs (Table 3). The lower concentrations imply a high degree of melt extraction during the period that the continental lithospheric mantle was still hot and capable of melting, and supports the hypothesis that frequent melting events occurred at this depth at some point in the past. Interestingly, individual analyses of phlogopite and carbonate minerals from peridotite xenoliths also have lower concentrations of these trace elements, suggesting they equilibrated with the host peridotite. The overlap between phlogopite and carbonate minerals with the MLXs suggests that the chemical variation seen in these xenoliths might be due to the presence of these minerals in the region of the MLD. If phlogopite and carbonate minerals in the mantle tend to form where fluid is concentrated and partial melting is a mechanism to concentrate fluids, than the presence of these minerals could represent a stalled crystallized melt, which could be responsible for the shear velocity decrease observed at the MLD.

5.4. Relationship to the LAB

In several different studies, the detection of a sharp seismic discontinuity near the depth of the expected transition in rheological properties across the LAB has been proposed to be evidence for a zone of collected or ponded melt at the base of the lithosphere [e.g., *Holtzmann et al*., 2003; *Kawakatsu et al*., 2009; *Sakamaki et al*., 2013]. Our model is similar in that it calls on magmas formed within cratonic lithosphere at or near the same depth that the LAB is observed near active margins. Melt is produced across a range of depths and migrates upward along grain boundaries until it encounters a permeability barrier [*Hebert and Montési*, 2010]. If melt is not erupted to the surface or emplaced into the lithosphere through diking, any remnant trapped melt will crystallize in place as the lithosphere cools. The MLD, therefore, may be the fingerprint of a chemical boundary that developed where the LAB had a past episode of active ponded melt and/or deposition of hydrous minerals by subduction (Figure 10). This model explains the presence of carbonate-rich metasomatism (short of carbonatite melts) occurring at depths associated with the LAB at active margins [*Delpech et al*., 2004; *Coltorti et al*., 1999; *Ionov et al*., 1993; *Yaxley et al*., 1998] and provides an additional mechanism for explaining the similar depths of LAB at active margins and the depths associated with MLD at inactive craton interiors. Alternatively, it provides a mechanism for concentrating hydrous minerals near the depth of the MLD, allowing for grain-boundary sliding weakening the shear modulus of hydrated mineralogies [*Karato*, 2012; *Olugboji et al*., 2013]. A primary limiting factor on our ability to further test this model is that seismic studies of the MLD and xenolith sampling across the interface are geographically incomplete. Future studies combining observations from both disciplines will provide a powerful indicator for further investigation of our model and others.

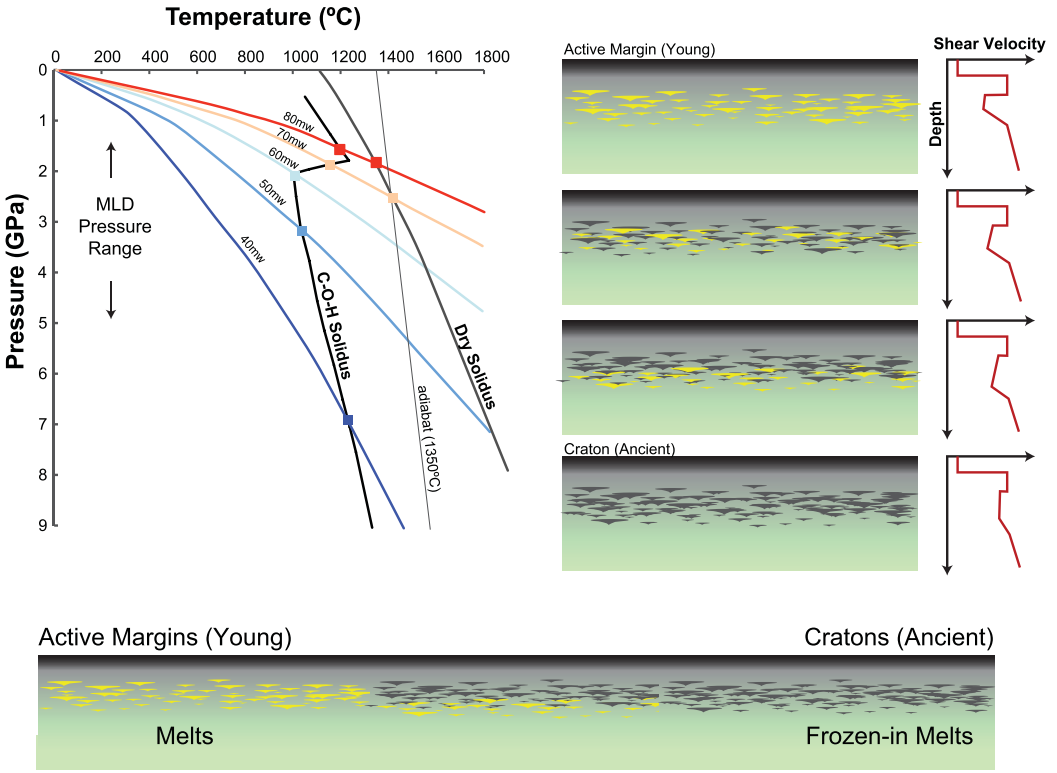

Figure 10. Conceptual model for the formation of a trapped melt layer solidifying in ancient crust and creating a chemical boundary at a depth consistent with the present-day MLD. Geothermal gradients illustrate the evolution of crust from hot (80 mW m^{-2}) to cold continental (40 mW m^{-2}) lithosphere that passes through a vapor-saturated solidus in the pressure-temperature diagram. The near horizontal kink in the solidus near 1.5 GPa would results in a permeability boundary for ascending melt, concentrating melt at a narrow horizon. This is graphically represented on the left as the lithosphere cools. The MLD would begin as a physical boundary between the lithosphere and asthenosphere, but as the mantle cools, the LAB would deepen, while the chemical signature of the MLD remains as the same depth.

6. Conclusions

We explored the hypothesis that a seismic velocity decrease observed between 60 and 150 km beneath continental lithosphere older than 1 Ga represents a chemical boundary within the mantle lithosphere. An examination of the xenolith database for samples attributed to regions with a seismically observed MLD shows the mineral phlogopite is present at the depth of the MLD. These xenoliths also have trace element concentrations that mimic phlogopite and carbonate minerals in mildly incompatible elements such as Zr, Lu, Ho, Yb, Y, and Er. However, high levels of Rb and Ba (which would be expected with high levels of phlogopite) are not present, suggesting the proportions of these minerals is fairly low. The addition of 5–15% phlogopite reduces the shear velocity of a peridotite to that observed at the MLD. Carbonate minerals have also been reported in the mantle, and show similar trace element concentrations to those found in xenoliths from the proposed MLD horizon. These xenoliths also indicate a higher degree of melting during their history shown by the depleted mildly incompatible trace elements.

We propose the following mechanism to explain these observations: a chemically distinct layer forms at ~65–90 km depth where crystallizing volatile-rich melt hits the solidus as it ascends and thermally equilibrates with the surrounding mantle. The near-horizontal volatile-rich solidus at 2 GPa fixes the crystallization of these melts at a consistent depth, and is preserved as continental lithosphere cools over geologic time. This implies the MLD arises from the LAB, whereas the LAB continues to deepen with time and thermal cooling of the lithosphere. Our models require that the two boundaries should coincide in regions of active melt generation in the mantle. If correct, this hypothesis predicts the MLD is a remnant indicator of the early evolution of continental lithosphere, in particular cratonic lithosphere, and links seismic velocity perturbations to mineralogy within the mantle.

Acknowledgments
This research originated as part of a small discussion group at the 2013 CIDER workshop at the University of California at Berkeley. We thank the following for their significant help in organizing and enhancing our discussions at the workshop: B. Romanowicz, R. Dasgupta, D. Schutt, K. Rychert, N. Harmon, C. Jaupart. I. Artemieva, R. Carlson, B., Stern, and L. Wagner. We particularly thank M. Hirschmann, C. Lee, J. Blichert-Toft, K. Fischer, and two additional anonymous reviewers who provided insightful comments and reviews that have greatly improved the manuscript. We also thank E. Van Allen for assistance with this article. All data used in this study can be found by tracing the references herein. Petrologic data were acquired from PetDB and can be searched for using the sample names provided. CIDER support for the authors comes from the National Science Foundation. N. Schmerr was supported by NSF grants EAR-1247608 and EAR-1361325. E. Emry was supported by NSF grant EAR-1349684. The GMT software [*Wessel and Smith*, 1998] was used for preparation of the figures. Data are accessible from the cited references within the text.

References

Abt, D. L., K. M. Fischer, S. W. French, H. A. Ford, H. Yuan, and B. Romanowicz (2010), North American lithospheric discontinuity structure imaged by Ps and Sp receiver functions, *J. Geophys. Res.*, *115*, B09301, doi:10.1029/2009JB006914.

Adams, A., and A. Nyblade (2011), Shear wave velocity structure of the southern African upper mantle with implications for the uplift of southern Africa, *Geophys. J. Int.*, *186*, 808–824.

Adams, A., A. Nyblade, and D. Weeraratne (2012), Upper mantle shear wave velocity structure beneath the East African plateau: Evidence for a deep, plateau wide low velocity anomaly, *Geophys. J. Int.*, *189*(1), 123–142.

Agashev, A. M., D. A. Ionov, N. P. Pokhilenko, A. V. Golovin, Y. Cherepanova, and I. S. Sharygin (2013), Metasomatism in lithospheric mantle roots: Constraints from whole-rock and mineral chemical composition of deformed peridotite xenoliths from kimberlite pipe Udachnaya, *Lithos*, *160*, 201–215.

Arculus, R. J., J. Ferguson, B. W. Chappell, D. Smith, M. T. McCulloch, I. Jackson, H. D. Hensel, S. R. Taylor, J. Knutson, and D. A. Gust (1988), Trace element and isotopic characteristics of eclogites and other xenoliths derived from the lower continental crust of southeastern Australia and southwestern Colorado Plateau, USA, in *Eclogites and Eclogite-Facies Rocks*, edited by D. C. Smith, pp. 335–386, Elsevier, Amsterdam.

Aulbach, S., W. L. Griffin, N. J. Pearson, and S. Y. O'Reilly (2013), Nature and timing of metasomatism in the stratified mantle lithosphere beneath the central Slave craton (Canada), *Chem. Geol.*, *352*, 153–169.

Bailey, D. K. (1990), Mantle carbonatite eruptions: Crustal context and implications, *Lithos*, *26*(1), 37–42.

Bali, E., A. Zanetti, C. Szabó, D. W. Peate, and T. E. Waight (2008), A micro-scale investigation of melt production and extraction in the upper mantle based on silicate melt pockets in ultramafic xenoliths from the Bakony–Balaton Highland Volcanic Field (Western Hungary), *Cont. Mineral. Petrol.*, *155*(2), 165–179.

Beghein, C., K. Yuan, N. Schmerr, and Z. Xing (2014), Changes in seismic anisotropy shed light on the nature of the Gutenberg discontinuity. *Science*, *343*(6176), 1237–1240.

Blundy, J., and J. Dalton (2000), Experimental comparison of trace element partitioning between clinopyroxene and melt in carbonate and silicate systems, and implications for mantle metasomatism, *Cont. Mineral. Petrol.*, *139*(3), 356–371.

Bodin, T., H. Yuan, and B. Romanowicz (2014), Inversion of receiver functions without deconvolution: Application to the Indian craton, *Geophys. J. Int.*, *196*, 1025–1033.

Brey, G. P., and T. Köhler (1990), Geothermobarometry in four-phase lherzolites II. New thermobarometers, and practical assessment of existing thermobarometers. *J. Petrol.*, *31*(6), 1353–1378.

Cammarano, F., and B. Romanowicz (2007), Insights into the nature of the transition zone from physically constrained inversion of long-period seismic data, *Proc. Natl. Acad. Sci. U. S. A.*, *104*(22), 9139–9144.

Carlson, R. W., and R. O. Moore (2004), Age of the eastern Kaapvaal mantle: Re-Os isotope data for peridotite xenoliths from the Monastery kimberlite, *S. Afr. J. Geol.*, *107*(1–2), 81–90.

Carlson, R. W., A. J. Irving, and B. C. Hearn Jr. (1999), Chemical and isotopic systematics of peridotite xenoliths from the Williams kimberlite, Montana: Clues to processes of lithosphere formation, modification and destruction, in *Proceedings of the VIIth International Kimberlite Conference*, vol. 1, Red Roof Design, edited by J. J. Gurney, et al., pp. 90–98, Cape Town.

Chakhmouradian, A. R., A. H. Mumin, A. Demény, and B. Elliott (2008), Postorogenic carbonatites at Eden Lake, Trans-Hudson Orogen (northern Manitoba, Canada): Geological setting, mineralogy and geochemistry. *Lithos*, *103*(3), 503–526.

Chu, R., B. Schmandt, and D. V. Helmberger (2012), Upper mantle P velocity structure beneath the Midwestern United States derived from triplicated waveforms, *Geochem. Geophys. Geosyst.*, *13*, Q0AK04, doi:10.1029/2011GC003818

Coltorti, M., C. Bonadiman, R. W. Hinton, F. Siena, and B. G. J. Upton (1999), Carbonatite metasomatism of the oceanic upper mantle: Evidence from clinopyroxenes and glasses in ultramafic xenoliths of Grande Comore, Indian Ocean, *J. Petrol.*, *40*(1), 133–165.

Connolly, J. A. D. (2005), Computation of phase equilibria by linear programming: A tool for geodynamic modeling and its application to subduction zone decarbonation, *Earth Planet. Sci. Lett.*, *236*, 524–541.

Courtier, A. M., and J. Revenaugh (2006), A water-rich transition zone beneath the eastern United States and Gulf of Mexico from multiple ScS reverberations, *Geophys. Monogr. Ser.*, *168*, 181–193.

Cvetković, V., M. Lazarov, H. Downes, and D. Prelević (2007), Modification of the subcontinental mantle beneath East Serbia: Evidence from orthopyroxene-rich xenoliths, *Lithos*, *94*(1), 90–110.

Danchin, R. V. (1979), Mineral and bulk chemistry of garnet lherzolite and garnet harzburgite xenoliths from the Premier Mine, South Africa, in *The Mantle Sample: Inclusion in Kimberlites and Other Volcanics*, edited by F. R. Boyd and H. O. A. Meyer, pp. 104–126, AGU, Washington, D. C.

Darbyshire, F. A., D. W. Eaton, and I. D. Bastow (2013), Seismic imaging of the lithosphere beneath Hudson Bay: Episodic growth of the Laurentian mantle keel, *Earth Planet. Sci. Lett.*, *373*, 179–193.

Dasgupta, R., and M. M. Hirschmann (2007), A modified iterative sandwich method for determination of near-solidus partial melt compositions. II. Application to determination of near-solidus melt compositions of carbonated peridotite, *Cont. Mineral. Petrol.*, *154*(6), 647–661.

Dasgupta, R., and M. M. Hirschmann (2010), The deep carbon cycle and melting in Earth's interior, *Earth Planet. Sci. Lett.*, *298*(1), 1–13.

Dasgupta, R., M. M. Hirschmann, W. F. McDonough, M. Spiegelman, and A. C. Withers (2009), Trace element partitioning between garnet lherzolite and carbonatite at 6.6 and 8.6 GPa with applications to the geochemistry of the mantle and of mantle-derived melts, *Chem. Geol.*, *262*(1), 57–77.

Dasgupta, R., A. Mallik, K. Tsuno, A. C. Withers, G. Hirth, and M. M. Hirschmann (2013), Carbon-dioxide-rich silicate melt in the Earth/"s upper mantle, *Nature*, *493*(7431), 211–215.

Dawson, J. B. (1999), Metasomatism and melting in spinel peridotite xenoliths from Labait, Tanzania, in edited by J. J. Gurney, et al., *Proc. 7th Int. Kimberlite Conf.*, vol. 1, *Red Roof Design*, pp. 164–173, Cape Town.

Deines, P., and D. P. Gold (1973), The isotopic composition of carbonatite and kimberlite carbonates and their bearing on the isotopic composition of deep-seated carbon. *Geochim. Cosmochim. Acta*, *37*(7), 1709–1733.

Delpech, G., M. Grégoire, S. Y. O'Reilly, J. Y. Cottin, B. Moine, G. Michon, and A. Giret (2004), Feldspar from carbonate-rich silicate metasomatism in the shallow oceanic mantle under Kerguelen Islands (South Indian Ocean), *Lithos*, *75*(1), 209–237.

Demény, A., T. W. Vennemann, E. Hegner, G. Nagy, J. A. Milton, A. Embey-Isztin, Z. Homonnay and G. Dobosi (2004), Trace element and C–O–Sr–Nd isotope evidence for subduction-related carbonate–silicate melts in mantle xenoliths (Pannonian Basin, Hungary). *Lithos*, *75*(1), 89–113.[Available at http://dx.doi.org/10.1016/j.lithos.2003.12.016.]

Doucet, L. S., D. A. Ionov, A. V. Golovin, and N. P. Pokhilenko (2012), Depth, degrees and tectonic settings of mantle melting during craton formation: Inferences from major and trace element compositions of spinel harzburgite xenoliths from the Udachnaya kimberlite, central Siberia, *Earth Planet. Sci. Lett.*, *359*, 206–218.

Duke, G. I. (2009). Black Hills–Alberta carbonatite–kimberlite linear trend: Slab edge at depth?, *Tectonophysics*, *464*(1), 186–194.
Ehrenberg, S. N. (1982), Rare earth element geochemistry of garnet lherzolite and megacrystalline nodules from minette of the Colorado Plateau province, *Earth Planet. Sci. Lett.*, *57*(1), 191–210.
Falloon, T. J., and D. H. Green (1989), The solidus of carbonated, fertile peridotite, *Earth Planet. Sci. Lett.*, *94*(3), 364–370.
Falus, G., C. Szabó, I. Kovács, Z Zajacz, and W. Halter (2007), Symplectite in spinel lherzolite xenoliths from the Little Hungarian Plain, Western Hungary: A key for understanding the complex history of the upper mantle of the Pannonian Basin, *Lithos*, *94*(1), 230–247.
Fischer, K. M., H. A. Ford, D. L. Abt, and C. A. Rychert (2010), The lithosphere-asthenosphere boundary, *Annu. Rev. Earth Planet. Sci.*, *38*, 551–575, doi:10.1146/annurev-earth-040809-152438.
Fishwick, S. (2010), Surface wave tomography: Imaging of the lithosphere-asthenosphere boundary beneath central and southern Africa?, *Lithos*, *120*, 63–73.
Fishwick, S., and N. Rawlinson (2012), 3-D structure of the Australian lithosphere from evolving seismic datasets, *Aust. J. Earth Sci.*, *59*(6), 809–826.
Flanagan, M. P., and Shearer, P. M. (1998), Global mapping of topography on transition zone velocity discontinuities by stacking SS precursors, *J. Geophys. Res.*, *103*(B2), 2673–2692.
Ford, H. A., K. M. Fischer, D. L. Abt, C. A. Rychert, and L. T. Elkins-Tanton (2010), The lithosphere–asthenosphere boundary and cratonic lithospheric layering beneath Australia from Sp wave imaging, *Earth Planet. Sci. Lett.*, *300*(3), 299–310.
Foster, K., K. Dueker, B. Schmandt, and H. Yuan (2014), A sharp cratonic lithosphere-asthenosphere boundary beneath the American Midwest and its relation to mantle flow, *Earth Planet. Sci. Lett.*, *402*, 82–89.
Francis, D. M. (1976), Amphibole pyroxenite xenoliths: Cumulate or replacement phenomena from the upper mantle, Nunivak Island, Alaska, *Cont. Mineral. Petrol.*, *58*(1), 51–61.
Franz, L., and R. L. Romer (2010), Different styles of metasomatic veining in ultramafic xenoliths from the TUBAF Seamount (Bismarck Microplate, Papua New Guinea). *Lithos*, *114*(1), 30–53.
Geissler, W. H., F. Sodoudi, and R. Kind (2010), Thickness of the central and eastern European lithosphere as seen by S receiver functions, *Geophys. J. Int.*, *181*(2), 604–634.
Glaser, S. M., S. F. Foley, and D. Günther (1999), Trace element compositions of minerals in garnet and spinel peridotite xenoliths from the Vitim volcanic field, Transbaikalia, eastern Siberia. *Lithos*, *48*(1), 263–285.
Green, D. H., W. O. Hibberson, A. Rosenthal, I. Kovács, G. M. Yaxley, T. J. Falloon, and F. Brink (2014), Experimental study of the influence of water on melting and phase assemblages in the upper mantle, *J. Petrol.*, *55*(10), 2067–2096.
Green, T. H., J. Adam, and S. H. Siel (1992), Trace element partitioning between silicate minerals and carbonatite at 25 kbar and application to mantle metasomatism, *Mineral. Petrol.*, *46*(3), 179–184.
Griffin, W. L., S. Y. O'Reilly, J. C. Afonso, and G. C. Begg (2009), The composition and evolution of lithospheric mantle: A re-evaluation and its tectonic implications, *J. Petrol.*, *50*(7), 1185–1204.
Gu, Y., A. M. Dziewonski, and C. B. Agee (1998). Global de-correlation of the topography of transition zone discontinuities, *Earth Planet. Sci. Lett.*, *157*(1), 57–67.
Hacker, B. R., G. A. Abers, and S. M. Peacock (2003), Subduction factory 1. Theoretical mineralogy, densities, seismic wave speeds, and H2O contents, *J. Geophys. Res.*, *108*(B1), 2029, *doi*:10.1029/2001JB001127.
Hansen, S. E., A. A. Nyblade, J. Julià, P. H. G. M. Dirks, and R. J. Durrheim (2009), Upper-mantle low-velocity zone structure beneath the Kaapvaal craton from S-wave receiver functions, *Geophys. J. Int.*, *178*, 1021–1027.
Hansen, S. M., K. G. Dueker, J. C. Stachnik, R. C. Aster, and K. E. Karlstrom (2013), A rootless rockies: Support and lithospheric structure of the Colorado Rocky Mountains inferred from CREST and TA seismic data, *Geochem. Geophys. Geosyst.*, *14*, 2670–2695, doi:10.1002/ggge.20143.
Hebert, L. B. and L. G. J. Montési (2010), Generation of permeability barriers during melt extraction at mid-ocean ridges, *Geochem. Geophys. Geosyst.*, *11*, Q12008, doi:10.1029/2010GC003270.
Heeszel, D. S., D. A. Wiens, A. A. Nyblade, S. E. Hansen, M. Kanao, M. An, and Y. Zhao (2013), Rayleigh wave constraints on the structure and tectonic history of the Gamburtsev Subglacial Mountains, East Antarctica, *J. Geophys. Res. Solid Earth*, *118*, 2138–2153, doi:10.1002/jgrb.50171.
Heit, B., F. Sodoudi, X. Yuan, M. Bianchi, and R. Kind (2007), An S receiver function analysis of the lithospheric structure in South America, *Geophys. Res. Lett.*, *34*, L14307, doi:10.1029/2007GL030317.
Heit, B., X. Yuan, M. Bianchi, R. Kind, and J. Gossler (2010), Study of the lithospheric and upper-mantle discontinuities beneath eastern Asia by SS precursors, *Geophys. J. Int.*, *183*(1), 252–266.
Helffrich, G., J. M. Kendall, J. O. S. Hammond, and M. R. Carroll (2011), Sulfide melts and long-term low seismic wave speeds in lithospheric and asthenospheric mantle, *Geophys. Res Lett.*, *38*, *L11301*, *doi*:10.1029/2011GL047126.
Holtzman, B. K., D. L. Kohlstedt, M. E. Zimmerman, F. Heidelbach, K. Hiraga, and J. Hustoft (2003), Melt segregation and strain partitioning: Implications for seismic anisotropy and mantle flow, *Science*, *301*, 1227–1230.
Hopper, E., H. A. Ford, K. M. Fischer, V. Lekic, and M. J. Fouch (2014), The lithosphere-athenosphere boundary and the tectonic and magmatic history of the northwestern United States, *Earth Planet. Sci. Lett.*, *402*, 69–81.
Humphreys, E. R., K. Bailey, C. J. Hawkesworth, F. Wall, J. Najorka, and A. H. Rankin (2010), Aragonite in olivine from Calatrava, Spain: Evidence for mantle carbonatite melts from> 100 km depth, *Geology*, *38*(10), 911–914.
Ionov, D. A., C. Dupuy, S. Y. O'Reilly, M. G. Kopylova, and Y.S. Genshaft (1993), Carbonated peridotite xenoliths from Spitsbergen: Implications for trace element signature of mantle carbonate metasomatism, *Earth Planet. Sci. Lett.*, *119*(3), 283–297.
Ionov, D. A., S. Y. O'Reilly, Y. S. Genshaft, and M. G. Kopylova (1996), Carbonate-bearing mantle peridotite xenoliths from Spitsbergen: Phase relationships, mineral compositions and trace-element residence, *Cont. Mineral. Petrol.*, *125*(4), 375–392.
Ionov, D. A., I. Ashchepkov, and E. Jagoutz (2005), The provenance of fertile off-craton lithospheric mantle: Sr–Nd isotope and chemical composition of garnet and spinel peridotite xenoliths from Vitim, Siberia, *Chem. Geol.*, *217*(1), 41–75.
Ita, J., and L. Stixrude (1992). Petrology, elasticity, and composition of the mantle transition zone, *J. Geophys. Res.*, *97*(B5), 6849–6866.
Janak, M., N. Froitzheim, M. Vrabec, E. J. Krogh Ravna, and J. C. M. Hoog (2006), Ultrahigh-pressure metamorphism and exhumation of garnet peridotite in Pohorje, Eastern Alps, *J. Metamorph. Geol.*, *24*(1), 19–31.
Jaupart, C., and J. C. Mareschal (1999), The thermal structure and thickness of continental roots, *Lithos*, *48*, 93–114.
Jiang, M., Y. Ai, L. Chen, and Y. Yang (2013), Local modification of the lithosphere beneath the central and western North China Craton: 3-D constraints from Rayleigh wave tomography, *Gondwana Res.*, *24*(3), 849–864.
Jones, A. P., M. Genge, and L. Carmody (2013), Carbonate melts and carbonatites, *Rev. Mineral. Geochem.*, *75*, 289–322.
Karato, S. (2012), On the origin of the asthenosphere, *Earth Planet. Sci. Lett.*, *321-322*, 95–103.
Karato, S. I. (2014), Does partial melting explain geophysical anomalies?, *Phys. Earth Planet. Inter.*, *228*, 300–306, doi:10.1016/j.pepi.2013.08.006.

Karato, S., T. Olugboji, and J. Park (2015), Mechanisms and geologic significance of the mid-lithospheric discontinuity in the continents, *Nat. Geosci.*, *8*, 509–514.
Kawakatsu, H., P. Kumar, Y. Takei, M. Shinohara, T. Kanazawa, E. Araki, and K. Suyehiro (2009), Seismic evidence for sharp lithosphere–asthenosphere boundaries of oceanic plates, *Science*, *324*, 499–502.
Kelemen, P. B., K. Hanghøj, and A. R. Greene (2003), One view of the geochemistry of subduction-related magmatic arcs, with an emphasis on primitive andesite and lower crust, *Treat. Geochem.*, *3*, 593–659.
Kempton, P. D., H. Downes, E. V. Sharkov, V. R. Vetrin, D. A. Ionov, D. A. Carswell, and A. Beard (1995), Petrology and geochemistry of xenoliths from the Northern Baltic shield: Evidence for partial melting and metasomatism in the lower crust beneath an Archaean terrane, *Lithos*, *36*(3), 157–184.
Kind, R., X. Yuan, and P. Kumar (2012), Seismic receiver functions and the lithosphere–asthenosphere boundary, *Tectonophysics*, *536*, 25–43. doi:10.1016/j.tecto.2012.03.005.
Kind, R., et al. (2013), Scandinavia: A former Tibet?, *Geochem. Geophys. Geosyst.*, *14*, 4479–4487, doi:10.1002/ggge.20251.
Kind, R., X. Yuan, J. Mechie, and F. Sodoudi (2015), Structure of the upper mantle in the north-western and central United States from USArray S-receiver functions, *Solid Earth Disscuss.*, *7*, 1025–1057, doi:10.5194/sed-7-1025-2015.
Kopylova, M. G., and J. K. Russell (2000), Chemical stratification of cratonic lithosphere: Constraints from the Northern Slave craton, Canada, *Earth Planet. Sci. Lett.*, *181*(1), 71–87.
Kopylova, M. G., J. K. Russell, and H. Cookenboo (1999), Petrology of peridotite and pyroxenite xenoliths from the Jericho kimberlite: Implications for the thermal state of the mantle beneath the Slave craton, northern Canada, *J. Petrol.*, *40*(1), 79–104.
Kumar, P., et al. (2005a), The lithosphere-asthenosphere boundary in the North-West Atlantic region, *Earth Planet. Sci. Lett.*, *236*, 249–257.
Kumar, P., X. Yuan, R. Kind, and G. Kosarev (2005b), The lithosphere-asthenosphere boundary in the Tien Shan-Karakoram region from S receiver functions: Evidence for continental subduction, *Geophys. Res. Lett.*, *32*, L07305, doi:10.1029/2004GL022291.
Kumar, P., X. Yuan, M. R. Kumar, R. Kind, X. Li, and R. K. Chadha (2007), The rapid drift of the Indian tectonic plate, *Nature*, *449*, 894–897, doi:10.1038/nature06214.
Kumar, P., X. Yuan, R. Kind, and J. Mechie (2012), The lithosphere-asthenosphere boundary observed with USArray receiver functions, *Solid Earth*, *3*, 149–159.
Lee, C. T., and R. L. Rudnick (1999), Compositionally stratified cratonic lithosphere: petrology and geochemistry of peridotite xenoliths from the Labait volcano, Tanzania, in edited by J. J. Gurney, *Proc. 7th Int. Kimberlite Conf.*, vol. 1, Red Roof Design, pp. 503–521, Cape Town.
Lee, C. T., R. L. Rudnick, W. F. McDonough, and I. Horn (2000), Petrologic and geochemical investigation of carbonates in peridotite xenoliths from northeastern Tanzania, *Cont. Mineral. Petrol.*, *139*(4), 470–484.
Lee, W. J., and P. J. Wyllie (1997). Liquid immiscibility between nephelinite and carbonatite from 1.0 to 2.5 GPa compared with mantle melt compositions, *Cont. Mineral. Petrol.*, *127*(1-2), 1–16.
Lehnert, K., Y. Su, C. H. Langmuir, B. Sarbas, and U. Nohl (2000), A global geochemical database structure for rocks, *Geochem. Geophys. Geosyst.*, *1*(5), doi:10.1029/1999GC000026.
Lekic, V., and K. M. Fischer (2014), Contrasting lithospheric signatures across the western United States revealed by Sp receiver functions, *Earth Planet. Sci. Lett.*, *402*, 90–98.
Levin, V., and J. Park (1997), P-SH conversions in a flat-layered medium with anisotropy of arbitrary orientation, *Geophys. J. Int.*, *131*, 253–266.
Litasov, K. D., S. F. Foley, and Y. D. Litasov (2000), Magmatic modification and metasomatism of the subcontinental mantle beneath the Vitim volcanic field (East Siberia): Evidence from trace element data on pyroxenite and peridotite xenoliths from Miocene picrobasalt, *Lithos*, *54*(1), 83–114.
Loock, G., H. G. Stosch, and H. A. Seck (1990), Granulite facies lower crustal xenoliths from the Eifel, West Germany: Petrological and geochemical aspects, *Cont. Mineral. Petrol.*, *105*(1), 25–41.
Lucassen, F., G. Franz, J. Viramonte, R. L. Romer, P. Dulski, and A. Lang (2005), The late Cretaceous lithospheric mantle beneath the Central Andes: Evidence from phase equilibria and composition of mantle xenoliths. *Lithos*, *82*(3), 379–406.
Maggi, A., E. Debayle, K. Priestley, and G. Barruol (2006), Multimode surface waveform tomography of the Pacific Ocean: A closer look at the lithospheric cooling signature, *Geophys. J. Int.*, *166*(3), 1384–1397.
McKenzie, D. A. N., and R. K. O'nions (1991), Partial melt distributions from inversion of rare earth element concentrations, *J. Petrol.*, *32*(5), 1021–1091.
Michard, A. (1989), Rare earth element systematics in hydrothermal fluids, *Geochim. Cosmochim. Acta*, *53*(3), 745–750.
Michaut, C., C. Jaupart, and J. C. Mareschal (2009), Thermal evolution of cratonic roots. *Lithos*, *109*(1), 47–60.
Mierdel, K., H. Keppler, J. R. Smyth, and F. Langenhorst (2007), Water solubility in aluminous orthopyroxene and the origin of Earth's asthenosphere, *Science*, *315*(5810), 364–368.
Miller, M. S., and D. W. Eaton (2010), Formation of cratonic mantle keels by arc accretion: Evidence from S receiver functions, *Geophys. Res. Lett.*, *37*, L18305, doi:10.1029/2010GL044366.
Mukhopadhyay, B., and W. I. Manton (1994), Upper-mantle fragments from beneath the Sierra Nevada Batholith: Partial fusion, fractional crystallization, and metasomatism in a subduction related ancient lithosphere, *J. Petrol.*, *35*(5), 1417–1450.
Nettles, M., and A. M. Dziewoński (2008), Radially anisotropic shear velocity structure of the upper mantle globally and beneath North America, *J. Geophys. Res.*, *113*, B02303, doi:10.1029/2006JB004819.
Olugboji, T. M., S. I. Karato, and J. Park (2013), Structures of the oceanic lithosphere-asthenosphere boundary: Mineral physics modeling and seismological signatures, *Geochem. Geophys. Geosyst.*, *14*, 880–901, doi:10.1002/ggge.20086.
Orejana, D., C. Villaseca, and B. A. Paterson (2006), Geochemistry of pyroxenitic and hornblenditic xenoliths in alkaline lamprophyres from the Spanish Central System, *Lithos*, *86*(1), 167–196.
Porritt, R. W., M. S. Miller, and F. A. Darbyshire (2015), Lithospheric architecture beneath Hudson Bay, *Geochem. Geophys. Geosyst.*, *16*, 2262–2275, doi:10.1002/2015GC005845.
Poudjom Djomani, Y. H., S. Y. O'Reilly, W. L. Griffin, and P. Morgan (2001), The density structure of sub- continental lithosphere through time, *Earth Planet. Sci. Lett.*, *184*, 605–621.
Priestley, K., D. McKenzie, E. Debayle, and S. Pilidou (2008), The African upper mantle and its relationship to tectonics and surface geology, *Geophys. J. Int.*, *175*, 1108–1126.
Rehfeldt, T., S. F. Foley, D. E. Jacob, R. W. Carlson, and D. Lowry (2008), Contrasting types of metasomatism in dunite, wehrlite and websterite xenoliths from Kimberley, South Africa, *Geochim. Cosmochim. Acta*, *72*(23), 5722–5756.
Revenaugh, J., and T. H. Jordan (1991), Mantle layering from ScS reverberations: 1. Waveform inversion of zeroth-order reverberations, *J. Geophys. Res.*, *96*(B12), 19,749–19,762.

Revenaugh, J., and R. Meyer (1997), Seismic evidence of partial melt within a possibly ubiquitous low-velocity layer at the base of the mantle, *Science*, *277*(5326), 670–673.
Revenaugh, J., and S. A. Sipkin (1994), Mantle discontinuity structure beneath China, *J. Geophys. Res.*, *99*(B11), 21,911–21,927.
Rey, P. F., N. Coltice, and N. Flament (2014), Spreading continents kick-started plate tectonics, *Nature*, *513*(7518), 405–408, doi:10.1038/nature13728.
Rudnick, R. L., W. F. McDonough, and A. Orpin (1994), Northern Tanzanian peridotite xenoliths: A comparison with Kaapvaal peridotites and inferences on metasomatic interactions, in edited by H. O. A. Meyer, O. H. Leonardo, Kimberlites, related rocks and mantle xenoliths, Companhia de Recursos Minerais Spec. Publ. 1A, Brasilia, pp. 336–353.
Rychert, C. A., S. Rondenay, and K. M. Fischer (2007), P-to-S and S-to-P imaging of a sharp lithosphere-asthenosphere boundary beneath eastern North America, *J. Geophys. Res*, Solid *Earth (1978–2012)*, *112*(B8).
Rychert, C. A., and P. M. Shearer (2009), A global view of the lithosphere-asthenosphere boundary, *Science*, *324*, 495–498.
Rychert, C. A., and P. M. Shearer (2011), Imaging the lithosphere-asthenosphere boundary beneath the Pacific using SS waveform modeling, *J. Geophys. Res.*, *116*, B07307, doi:10.1029/2010JB008070.
Rychert, C. A., K. M. Fischer, and S. Rondenay (2005), A sharp lithosphere–asthenosphere boundary imaged beneath eastern North America, *Nature*, *436*(7050), 542–545.
Rychert, C. A., P. M. Shearer, and K. M. Fischer (2010), Scattered wave imaging of the lithosphere–asthenosphere boundary, *Lithos*, *120*(1), 173–185, doi:10.1016/j.lithos.2009.12.006.
Sakamaki, T., S. Akio, O. Eiji, T. Hidenori, U. Satoru, K. Yoshinori, F. Ken-ichi, W. Yanbin, W. H. John, and D. B. Maxim (2013), Ponded melt at the boundary between the lithosphere and asthenosphere, *Nat. Geosci. 6*(12), 1041–1044.
Saul, J., M. R. Kumar, and D. Sarkar (2000), Lithospheric and upper mantle structure of the Indian Shield, from teleseismic receiver functions, *Geophys. Res. Lett.*, *27*(16), 2357–2360.
Savage, B., and P. G. Silver (2008), Evidence for a compositional boundary within the lithospheric mantle beneath the Kalahari craton from S receiver functions, *Earth Planet. Sci. Lett.*, *272*(3), 600–609.
Savage, M. K. (1998). Lower crustal anisotropy or dipping boundaries? Effects on receiver functions and a case study in New Zealand, *J. Geophys. Res.*, *103*(B7), 15,069–15,087.
Schilling, M., R. V. Conceicao, G. Mallmann, E. Koester, K. Kawashita, F. Hervé, D. Morata, and A. Motoki (2005), Spinel-facies mantle xenoliths from Cerro Redondo, Argentine Patagonia: Petrographic, geochemical, and isotopic evidence of interaction between xenoliths and host basalt, *Lithos*, *82*(3), 485–502.
Schmerr, N. (2012), The Gutenberg Discontinuity: Melt at the Lithosphere-Asthenosphere Boundary, *Science*, *335*, 1480–1483.
Schmidberger, S. S., and D. Francis (2001), Constraints on the trace element composition of the Archean mantle root beneath Somerset Island, Arctic Canada, *J. Petrol.*, *42*(6), 1095–1117.
Selway, K., H. Ford, and P. Kelemen (2015), The seismic mid-lithosphere discontinuity, *Earth Planet. Sci. Lett.*, *414*, 45–57.
Shearer, P. M. (1990), Seismic imaging of upper-mantle structure with new evidence, *Nature*, *344*(8), 121–126.
Shearer, P. M. (1993), Global mapping of upper mantle reflectors from long-period SS precursors, *Geophys. J. Int.*, *115*(3), 878–904.
Snyder, D. B. (2008), Stacked uppermost mantle layers within the Slave craton of NW Canada as defined by anisotropic seismic discontinuities, *Tectonics*, *27*, TC4006, doi:10.1029/2007TC002132.
Sodoudi, F., X. Yuan, R. Kind, S. Lebedev, J. M.-C. Adam, E. Kästle, and F. Tilmann (2013), Seismic evidence for stratification in composition and anisotropic fabric within the thick lithosphere of Kalahari Craton, *Geochem. Geophys. Geosyst.*, *14*, 5393–5412, doi:10.1002/2013GC004955.
Soustelle, V., A. Tommasi, S. Demouchy, and D. A. Ionov (2010), Deformation and fluid–rock interaction in the supra-subduction mantle: Microstructures and water contents in peridotite xenoliths from the Avacha Volcano, Kamchatka, *J. Petrol.*, *51*(1-2), 363–394.
Sparks, D., and E. M. Parmentier (1991), Melt extraction from the mantle beneath spreading centers, *Earth Planet. Sci. Lett.*, *105*(4), 368–377, doi.org/10.1016/0012-821X(91)90178-K.
Sun, S. S., and W. McDonough (1989), Chemical and isotopic systematics of oceanic basalts: Implications for mantle composition and processes, *Geol. Soc. Spec. Publ.*, *42*(1), 313–345.
Thybo, H. (2006), The heterogeneous upper mantle low velocity zone, *Tectonophysics*, *416*, 53–79.
Thybo, H., and E. Perchuc (1997), The seismic 8° discontinuity and partial melting in continental mantle, *Science*, *275*, 1626–1629. doi: 10.1126/science.275.5306.1626.
Tonegawa, T., and G. Helffrich (2012), Basal reflector under the Philippine Sea Plate, *Geophys. J. Int.*, *189*, 659–668.
Wessel, P., and W. H. Smith (1998), New, improved version of Generic Mapping Tools released, *Eos Trans. AGU*, *79*(47), 579–579.
Wirth, E. A., and M. D. Long (2014), A contrast in anisotropy across mid-lithospheric discontinuities beneath the central United States: A relic of craton formation, *Geology*, *42*(10), 851–854, doi:10.1130/G35804.1.
Wittlinger, G., and V. Farra (2007), Converted waves reveal a thick and layered tectosphere beneath the Kalahari super-craton, *Earth Planet. Sci. Lett.*, *254*(3), 404–415.
Wölbern, I., G. Rümpker, K. Link, and F. Sodoudi (2012), Melt infiltration of the lower lithosphere beneath the Tanzania craton and the Albertine rift inferred from S receiver functions, *Geochem. Geophys. Geosyst.*, *13*, Q0AK08, doi:10.1029/2012GC004167.
Workman, R. K., and S. R. Hart (2005), Major and trace element composition of the depleted MORB mantle (DMM), *Earth Planet. Sci. Lett.*, *231*(1), 53–72.
Yaxley, G. M., D. H. Green, and V. Kamenetsky (1998), Carbonatite metasomatism in the southeastern Australian lithosphere, *J. Petrol.*, *39*(11-12), 1917–1930.
Yu, S. Y., Y. G. Xu, J. L. Ma, Y. F. Zheng, Y. S. Kuang, L. B. Hong, W.-C. Ge, and L. X. Tong (2010), Remnants of oceanic lower crust in the subcontinental lithospheric mantle: Trace element and Sr–Nd–O isotope evidence from aluminous garnet pyroxenite xenoliths from Jiaohe, Northeast China, *Earth Planet. Sci. Lett.*, *297*(3), 413–422.
Yuan, H., and B. Romanowicz (2010), Lithospheric layering in the North American craton, *Nature*, *466*, 1063–1069, doi:10.1038/nature09332.
Yuan, X., R. Kind, X. Li, and R. Wang (2006), The S receiver functions: Synthetics and data example, *Geophys. J. Int.*, *165*, 555–564, doi: 10.1111/j.1365-246X.2006.02885.x.
Yuan, H., B. Romanowicz, K. M. Fischer, and D. Abt (2011), 3-D shear wave radially and azimuthally anisotropic velocity model of the North American upper mantle, *Geophys. J. Int.*, *184*(3), 1237–1260.
Zhang, Z., and T. Lay (1993), Investigation of upper mantle discontinuities near northwestern Pacific subduction zones using precursors to sSH, *J. Geophys. Res.*, *98*(B3), 4389–4405.
Zheng, Z., and B. Romanowicz (2012), Do double 'SS precursors' mean double discontinuities?, *Geophys. J. Int.*, *191*(3), 1361–1373.